CONFESS

Consistent representation of temporal variations of boundary forcings in reanalyses and seasonal forecasts

Improved vegetation variability

Andrea Alessandri, Fransje van Oorschot

www.confess-h2020.eu

Co-ordinated by ECMWF

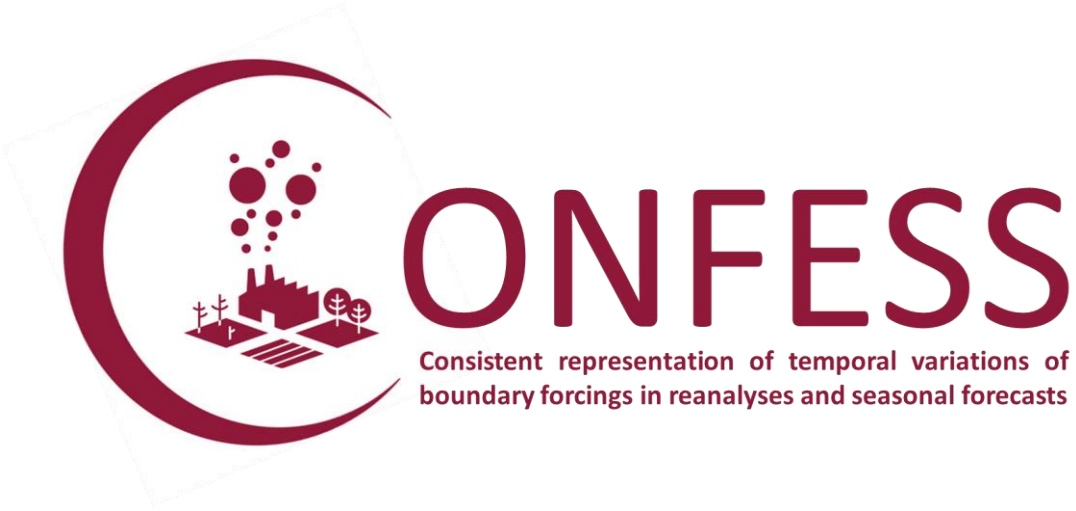

D1.2 Improved vegetation variability

Author(s): Fransje van Oorschot (CNR)
Andrea Alessandri (CNR)
Constantin Ardilouze (MF)
Gildas Dayon (MF)
Souhail Boussetta (ECMWF)
Gianpaolo Balsamo (ECMWF)
Melissa Ruiz-Vasquez (ECMWF, MPI-BGC)

Dissemination Level: Public/ Confidential

Date: 28/10/2022
Version: 3.0
Contractual Delivery Date: 31/10/2022
Work Package/ Task: WP1/ T1.2-and T1.3
Document Owner: CNR-ISAC
Contributors: CNR, ECMWF, MF
Status: Final report

CONFESS

Consistent representation of temporal variations of boundary forcings in reanalyses and seasonal forecasts

Research and Innovation Action (RIA)
H2020- LC-SPACE-18-EO-2020 Copernicus evolution: Research activities in support of the evolution of the Copernicus services - Copernicus Climate Change Service (C3S

Project Coordinator: Dr Magdalena Alonso Balmaseda (ECMWF)
Project Start Date: 01/11/2020
Project Duration: 36 months

Published by the CONFESS Consortium

Contact:
ECMWF, Shinfield Park, Reading, RG2 9AX, United Kingdom
Magdalena.Balmaseda@ecmwf.int

The CONFESS project has received funding from the European Union's Horizon 2020 research and innovation programme under grant agreement No 101004156.

Contents

Figures

Tables

1 Executive Summary

Land Cover and vegetation observations are of paramount importance to properly constrain the land surface models that are included in current reanalysis and seasonal-to-decadal prediction systems. In this deliverable, we present the integration of the unprecedented vegetation information, from the latest satellite campaigns in the frame of Copernicus, into the land surface models (LSMs) used for reanalysis and initialization of the seasonal to decadal prediction systems. Observational Land Cover (LC) and Leaf Area Index (LAI) from CONFESS deliverable D1-1 (Boussetta & Balsamo, 2021) are implemented as boundary conditions for the CHTESSEL (ECMWF), the EC-Earth HTESSEL-LPJGuess (CNR) and the ISBA-CTRIP (Météo-France) LSMs. Furthermore, a parameterization of the effective vegetation cover that is constrained using observations of FCover (Fraction of green Vegetation Cover) is developed and included in the EC-Earth HTESSEL-LPJGuess (CNR). The effects of the improved representation of vegetation variability from observations on the LSMs has been evaluated in offline simulations forced by ERA5 atmospheric forcing. The effects on the simulated water and energy fluxes are first evaluated by comparing the three individual LSMs, as used by the partners involved in WP1, with available observations. The multi-model comparison of the sensitivities is also evaluated to account for model differences in configuration and parameterizations. The results and knowledge from the sensitivity analysis in this deliverable is driving the selection of optimal solutions and configurations to include in the initialization/simulation of the predictions in CONFESS WP3 and will further guide future developments in land surface modeling for the next generation of operational seasonal and multi-annual prediction systems.

2 Introduction

2.1 Background

Vegetation variability at seasonal and inter-annual time scales strongly controls water and energy balances of the land surface. However, state-of-the-art land surface models (LSMs) included in short-term climate prediction systems (e.g. MeteoFrance and ECMWF SEAS5) do not account for realistic land cover (LC) and vegetation boundary conditions and do not include parameterizations able to interactively model seasonal to inter-annual variations in vegetation density. Specifically, LC does not change inter-annually in these LSMs, while it is well known to have been changing due to for example deforestation or vegetation shifts. Similarly, while the climatological seasonal variations in vegetation density (of which Leaf Area Index, LAI, is a proxy) are described in these LSMs, the inter-annual variations of LAI due for example to droughts are not represented. Realistic representation of inter-annual variations in LC and LAI are fundamental to adequately model the signal due to variations in land surface-atmosphere interactions. New observations and latest-generation vegetation data are therefore of paramount importance to properly constrain LSMs used for off-line analysis/initialization and for seasonal-to-decadal predictions done with fully coupled climate models.

2.2 Scope of this deliverable

2.2.1 Objectives of this deliverable

The objective of this deliverable is to integrate the unprecedented vegetation information, from the latest satellite campaigns in the frame of Copernicus, in the land surface models used for offline simulation and initialization of the prediction systems.

1.1.1 Work performed in this deliverable

The 'Vegetation dataset of Land Use/Land Cover and Leaf Area Index" developed in Deliverable 1.1 (from here referred to as D1-1; Boussetta & Balsamo, 2021) is exploited. The work performed in this deliverable can be summarized as follows:

- Model development
  - Development and technical work to implement boundary conditions from observational LAI and LC from D1-1.
  - Development of a parameterization of the effective vegetation cover as a function of LAI that is constrained using FCOVER observations (included in the EC-Earth HTESSEL-LPJGuess by CNR only).
- Model experiments
  - Offline land-surface model simulations using ERA5 atmospheric forcing and with the novel LAI and LC boundary conditions for improved representation of land surface-atmosphere interactions and for the initialization of the seasonal-to-decadal prediction systems.
  - Offline land-surface model simulations using ERA5 atmospheric forcing and with the improved parameterization of the effective vegetation cover as a function of LAI.
- Model evaluation

- The set of offline sensitivity simulations to the improved vegetation inter-annual variability by each partner are evaluated.
- In a multi-model comparison, the model sensitivities to the realistic inter-annual vegetation variability are evaluated.

2.2.2 Deviations and counter measures

No deviations have been encountered.

3 Methodology

3.1 Data description

Here we briefly describe the observational data of LU/LC, LAI and FCOVER that are used to constrain the modelling in WP1. Details of the development of the LU/LC and LAI data are described in CONFESS deliverable D1.1.

3.1.1 Land use / land cover data

The ESA-CCI/C3S land cover data was used and processed in D1-1 for application in the modelling presented in this report. The original 300m land cover classes were aggregated to the target resolution and converted to the IFS vegetation types using a cross walking table. The LC data was delivered at a yearly resolution from 1993-2019 by ECMWF in D1.1.

3.1.2 Leaf Area Index data

The LAI data from CGLS/C3S (SPOT sensor: 1999-2013 and PROBAV-sensor: 2014-2019) was harmonized with the AVHRR-based data (1993-1999) using a Cumulative Distribution Function (CDF) matching approach at a 1km resolution, using the methodology described in D1.1. For the ECMWF IFS and EC-Earth IFS models the LAI is disaggregated into high and low LAI based on the high and low vegetation fractions from the LC maps. The novel CGLS LAI data was delivered for different resolutions at a monthly resolution for 1993-2019 by ECMWF in D1.1.

3.1.3 Fraction of green vegetation data

In addition to LC and LAI data we used CGLS data of the Fraction of green Vegetation Cover (FCover), which describes the fraction of green vegetation per unit ground area. We obtained FCover from CGLS at a 10-daily temporal and 1km spatial resolution (Verger et al., 2019; https://land.copernicus.eu/global/products/fcover). We harmonised the 1999-2013 and 2014-2019 periods using CDF matching as described in D1.1 (Figure 1). The homogenized FCover data was used in combination with LAI and LC for the model development of effective vegetation cover parameterization (Section 3.2.3).

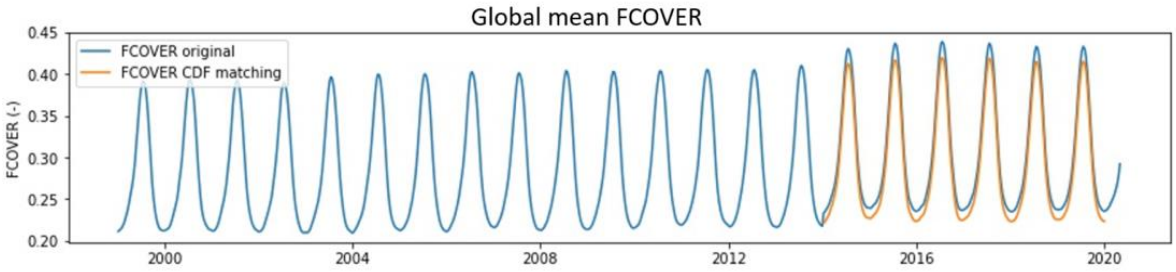

Figure 1 Global mean FCover of original data (blue) with SPOT sensor 1999-2013 and PROBA-V sensor 2014-2019, and homogenized data (orange) after applying CDF-matching to the 2014-2019 period.

3.2 Model description and developments

Here each partner describes the relevant model parameterization and developments within the project.

3.2.1 Meteo France model

The land surface model is ISBA-CTRIP (Decharme et al., 2019), embedded in the SURFEX modeling platform (Voldoire et al., 2017). This model version is the same as that used for CMIP6 simulations.

Description of the reference Land-Cover (ECOCLIMAP)

The land cover properties are specified according to the 1-km resolution ECOCLIMAP-II database (Faroux et al., 2013). More than 500 land cover units are derived from the Corine Land Cover map for the year 2000 at 100-m resolution over Europe and from the Global Land Cover 2000 database elsewhere. Theses land cover units are aggregated to the model resolution into 12 subgrid land tiles in order to account for land cover heterogeneities, 9 of them corresponding to vegetated land types.

Table 1. ISBA subgrid land types

Tiles	Land type
1	Bare soil & desert
2	Rock and urban area
3	Permanent snow and ice
4	Deciduous broadleaf trees & shrub
5	Needleleaf trees
6	Evergreen broadleaf trees
7	C3 crops
8	C4 crops
9	Irrigated crops
10	Boreal grassland
11	Tropical grassland
12	Peat bogs

The grid cell fraction of vegetation is fixed to 0 for deserts, rock and urban areas as well as permanent snow and ice, to 0.95 for grasslands, peat bogs and boreal forests and to 1 for tropical evergreen forests. For crop tiles, this fraction f varies with LAI as in the following equation:

$$f = 1 - e^{-0.6\mathrm{LAI}}$$

The ECOCLIMAP fixed land cover can be used with either a fixed or interactive LAI scheme.

Description of vegetation and carbon assimilation

Vegetation in the ISBA land surface scheme is represented by a maximum of six biomass reservoir of: leaves, stem/twigs, wood, fine and coarse roots, and a small additional storage pool.

The photosynthesis and associated carbon assimilation depend on the stomatal conductance of leaves (Jacobs, 1994, Calvet et al, 1998). In ISBA, this conductance is controlled by three factors: the atmospheric CO2 concentration, the atmospheric vapour pressure deficit (Joetzjer et al. 2015) and soil moisture availability. Finally, the soil water used for transpiration is removed throughout the root zone according to a vertical root-density profile.

Description of the fixed LAI scheme (ECOCLIMAP)

The climatological seasonal cycle of the LAI is imposed for each land cover unit at a 10-day time step. This seasonal-cycle climatology is computed using the collection 5 of the Moderate Resolution Imaging Spectroradiometer (MODIS) leaf area index product at 1-km spatial resolution combined with the Normalized Difference Vegetation Index product from the SPOT/Vegetation data set from 1 January 1999 to 31 December 2005.

Description of prescribed inter-annual LAI in CONFESS

The 1km LAI dataset described in section 3.1.2 was upscaled to the Tl127 grid by a bilinear interpolation and was disaggregated into vegetation types by conserving the same proportion of vegetation types by grid cell, as derived from ECOCLIMAP. Then, the LAI values are updated at each time step of the simulation with this dataset of interpolated 10-daily LAI values for the different vegetation types.

Description of the interactive LAI scheme

Leaf biomass is based on the carbon assimilated by photosynthesis and decreased by turnover, respiration, and allocation to the other pools (Gibelin et al.,2006). Leaf phenology results directly from the daily carbon balance of the leaves. Finally, LAI is diagnosed from leaf biomass (B) and specific Leaf area (SLA), which varies as a function of leaf nitrogen concentration and plant functional type:

$$LAI = B * SLA$$

The photosynthesis, respiration and carbon allocation schemes are further detailed in Delire et al. 2020.

3.2.2 ECMWF model

Tiled ECMWF Scheme for Surface Exchanges over Land (CHTESSEL, Balsamo et al., 2011, Boussetta et al., 2013). The land surface model version used in CONFESS is based on the 47R3 model cycle (https://www.ecmwf.int/en/elibrary/20198-ifs-documentation-cy47r3-part-iv-physical-processes).

In the current ECMWF land surface model (ECLand) and data assimilation system the land use/land cover (LULC) is processed from the Global Land Cover Characteristics data set (GLCC, Loveland et al., 2000) and the Leaf Area Index (LAI) is based on a 2000-2008 climatology from the Moderate Resolution Imaging Spectroradiometer (MODIS) collection 5 (MOD15A2) data. An observation operator that disaggregates the LAI into a high and low vegetation component is applied to the observed data to allow using it in the ECLand system. The observed LAI was rescaled using a static LAI dataset to guarantee neutral impact on the ECMWF model (Boussetta et al., 2013). These crucial input data do not fully benefit from new developments of vegetation related remote sensing vegetation data. Recent studies have identified limitations of the current land cover and LAI datasets used in ECLand (Johannsen et al., 2019) over several regions of the world.

Within CONFESS, the new ESA-CCI LULC and CGLS LAI (CONFESS D1.1) are used within ECLand to assess the impact of varying vegetation condition on the surface offline system in a first step and in the coupled system in a second phase within WP3.

3.2.3 CNR model

Model description

Here we use the Hydrology Tiled ECMWF Scheme for Surface Exchanges over Land (HTESSEL) land surface model (Balsamo et al., 2009) as it was modified and implemented in the EC-EARTH v3 Earth system model (Döscher et al., 2021). In HTESSEL the vegetated area of a grid cell is divided into high and low vegetation tiles, with in case of snow also separate model tiles for snow on bare ground/low vegetation and snow beneath high vegetation (Balsamo et al., 2009). Each high and low vegetation tile is described by the vegetation cover fraction and the dominant vegetation type. Originally, these vegetation parameters were defined by the GLCC land cover dataset (Loveland et al., 2000).

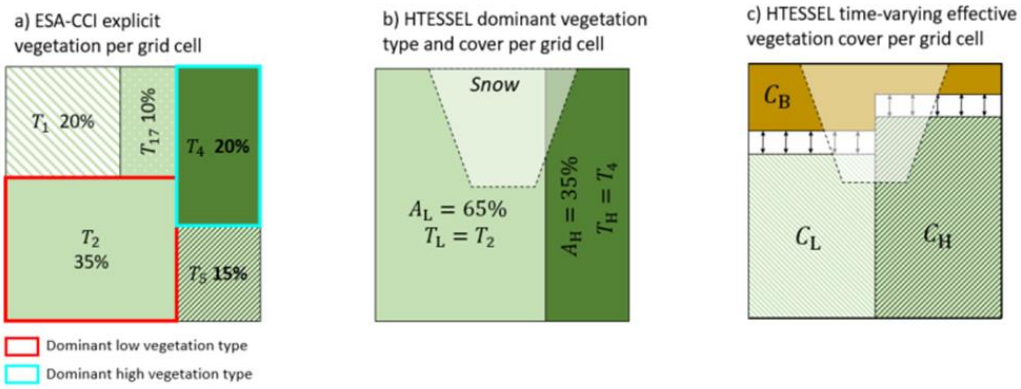

Figure 2 Grid cell vegetation description with example numbers. (a) ESA-CCI explicit vegetation fraction (b) HTESSEL dominant vegetation type and cover, (c) HTESSEL effective vegetation cover with CB bare soil cover, CL and CH low and high effective cover. Vegetation indices are given in Table 2.

The original HTESSEL model describes a seasonal cycle of LAI derived from a satellite-based climatology based on MODIS (Boussetta et al., 2013). In the model, the LAI controls the canopy resistance r_c through the following linear relation:

$$r_c = \frac{r_{s,min}}{LAI} f_1(R_s) f_2(D_a) f_3(\theta)$$

With $r_{s,min}$ the vegetation specific minimum canopy resistance and $f_1(R_s)$, $f_2(D_a)$, $f_3(\theta)$ functions describing the dependences on shortwave radiation (R_s), atmospheric water vapor deficit (D_a) and soil moisture (θ). The vegetation transpiration is linearly related to r_c and other atmospheric variables.

Furthermore, the LAI controls the capacity of the model interception reservoir W1m by:

$$W_{1m} = W_{1max} * \left(C_B + C_H * LAI(T_H) + C_L * LAI(T_L)\right)$$

With W1max=0.0002m and CB, CH and CL the fractions of bare soil, effective high and low vegetation, respectively (Section 2.3.3). The interception evaporation per time step follows from the water content of the interception reservoir (calculated from precipitation), and W1m the potential evaporation. The model effective high and low vegetation cover (CH and CL) represent the part of the model vegetation cover (AH and AL) that is actively contributing to the water balance through transpiration and interception evaporation. The fraction of the grid cell not covered by the effective vegetation is treated as bare soil (CB) where only soil evaporation takes place. CH, CL and CB are described by:

$$C_H = C_{v,H} \cdot A_H$$

$$C_L = C_{v,L} \cdot A_L$$

$$C_B = 1 - C_H - C_L$$

with CvH and CvL the vegetation density. Originally, CvH and CvL were described by a look-up table with vegetation specific values, allowing for spatial variation of the CH, CL and CB fractions. However, this approach does not allow for temporal variations in vegetation density, so the seasonal and inter-annual variability of vegetation effective cover is not represented. To overcome this limitation, the vegetation density was linked to the variability of LAI by the following exponential relation (Alessandri et al., 2017):

$$C_{v,L} = 1 - \exp(-k \cdot LAI_L)$$

$$C_{v,H} = 1 - \exp(-k \cdot LAI_H)$$

with k the canopy light extinction coefficient that represents the amount of vegetation clumping (Anderson, 2005).

Model developments

Implementation of latest generation land cover data

Here we apply the latest generation land cover data from ESA-CCI (Section 3.1.1). For application in HTESSEL the 300m data was aggregated to the model resolution T255 (~50x50km) and converted to the 10 vegetation types presented in Table 1 after applying the cross-walking table (D1-1). For each grid cell we obtain an explicit vegetation cover fraction for each vegetation type (Figure 2a). For some vegetation types (e.g. Crops and Deciduous broadleaf trees), the maximum explicit vegetation cover fraction is smaller than 1 because the cross-walking table used assumes that these vegetation types are always mixed with other vegetation types, and there is never a 100% cover (Table 2). In HTESSEL the explicit vegetation (Figure 2a) is converted to a dominant high and low vegetation type (TH and TL) and a total high and low vegetation fractional cover (AH and AL) (see Figure 2a,b for an example of this conversion).

The changes in TL and TH directly influences the model parameterization, because several model parameters that control surface water and energy fluxes (vegetation root distribution, minimum canopy resistance and roughness lengths for momentum and heat) are prescribed by look up tables based on vegetation type (ECMWF, 2021). Model evaporation is calculated separately for the high and the low vegetation tiles, and weighted by the CL and CH fractions to obtain total grid cell evaporation.

Table 2 HTESSEL vegetation types according to the IFS BATS LC classification and the maximum explicit vegetation cover defined by the cross-walking table.

Vegetation index	High /Low	Vegetation type	Maximum fractional cover
1	L	Crops, mixed farming	0.90
2	L	Short grass	1.00
3	H	Evergreen needleleaf trees	0.85
4	H	Deciduous needleleaf trees	0.75
5	H	Deciduous broadleaf trees	0.70
6	H	Evergreen broadleaf trees	0.90
9	L	Tundra	1.00
13	L	Bogs and marshes	0.75
16	L	Evergreen shrubs	0.70
17	L	Deciduous shrubs	0.70

Implementation of latest generation LAI data

Here we use the novel CGLS LAI data described in Section 3.1.2 to prescribe a realistic representation of both seasonal cycle and inter-annual variability of LAI. The 1km LAI data was remapped to the T255 grid by conservative interpolation and was disaggregated into low and high LAI for the use in the HTESSEL model setup with separate high and low vegetation tiles, based on the high and low vegetation cover fractions (AL and AH) **(**D1-1) (Figure 2b).

Improved parameterization of the effective vegetation cover using FCover data

Until now the canopy light extinction coefficient k was set to a constant value of 0.5 (Alessandri et al., 2017; Krinner et al., 2005) or 0.6 (Nogueira et al., 2020; Boussetta et al., 2021). However, the effect of vegetation clumping, and so the shape of this relation is different for different vegetation types (Chen et al., 2005; Chen, 2012; Ryu, 2010). Differently from other works, we estimate vegetation specific k-values using the satellite data of FCover and LAI (10-daily, 1km grid) together with the ESA-CCI land cover (yearly, 1km grid), as discussed in Section 3.1.
We assume here that FCover is analogous to the total model vegetation density (CVH+CVL), so the model-k can be estimated using:

$$FCover = 1 - exp(-k * LAI)$$

We fitted the CGLS FCover observations with this equation by solving for different values of the k-parameter for each vegetation type using a non-linear least squares optimization. To differentiate vegetation types, we selected grid cells with the maximum possible explicit vegetation fraction (Table 1) for each vegetation type, for each year. For these grid cells, the FCover and LAI 10-daily data for 1999-2019 were extracted. To make computational costs affordable while keeping a representative sample with robust significance of the fitting, we took a randomly selected subsample of grid points (2000) for each vegetation type of the LAI and FCover timesteps (10-daily). In this way we obtained for each vegetation type a sample of 2000 gridpoints * 36 timesteps per year * 20 years = 1 440 000 data points. The LAI and FCover values of these data points were combined and the estimate of k was optimized using a non-linear least squares optimization. To optimally isolate individual vegetation types, the parameter fitting was done at a 1km resolution using the explicit vegetation fractions from ESA-CCI and the total LAI. However, in the model the effective vegetation cover is calculated at a coarser spatial resolution, using disaggregated LAI for the dominant vegetation types.

3.3 Experiments

Table 3 summarizes the experimental set-up for the three institutes including spatial resolution, historical period covered, and LAI/LC configurations.

3.3.1 MF experimental setup

Offline simulations with Surfex (ISBA-CTRIP) were carried out at the tl127 resolution on a reduced Gaussian grid, and driven by hourly surface ERA5 fields upscaled at the same horizontal resolution. 4 different simulations were performed: (i) a control run with climatological LAI and the reference fixed land cover map, (ii) a run with interactive LAI and the reference fixed land cover map, (iii) a run where LAI evolves interactively and land cover map is updated every year and derived from LUH2 (Hurtt et al., 2011) version 2.0h, as described in Delire et al. (2020), and (iv) a fourth run where time-varying 1993-2019 CGLS LAI is used while keeping the reference fixed land cover map. All simulations but (iv) have been carried out for the period 1950-2019.

3.3.2 ECMWF experimental setup

Offline simulations with ECLand were carried out for the period 1993-2019 at the TL639 reduced Gaussian grid and driven by near-surface meteorological fields from the ECMWF ERA5 reanalysis having the same spatial resolution (Hersbach et al., 2020). The simulations are performed using 3 main configurations: (i) a control run with static 2019 ESA-CCI LULC maps and climatological CGLS LAI, (ii)) a second configuration where varying ESA-CCI LULC is used for the 1993-2019 period and LAI is climatological, (iii) a third configuration where time-varying 1993-2019 CGLS LAI is used while keeping the 2019 fixed LULC and (iv) a fourth configuration where both time-varying CGLS LAI and time-varying ESA-CCI LULC are used for the 1993-2019 period.

3.3.3 CNR experimental setup

CNR performed offline simulations with HTESSEL using hourly ERA5 forcing for 1993-2019, with 1980-1993 the spin-up period. In the spin-up the LAI was set to climatological values from CGLS 1993-2019 and LC to the values of ESA-CCI 1993. In the control experiment (ctr), the LAI and LC from the spin-up are also used for 1993-2019. In the LAI sensitivity experiment (pla) we replace the climatological LAI with the inter-annual varying CGLS LAI, keeping the LC fixed. The fixed LC is replaced by the multi-annual varying LC from ESA-CCI to evaluate the LC sensitivity (plalc). The model sensitivity to the updated effective cover parameterization was tested on top of the LAI and LC variability (plalc-kv). We evaluated the monthly mean output of these experiments.

Table 3. Details of experimental setup for CNR, MF and ECMWF models.

Institute	Experiment	Period	Spatial resolution	LAI configuration	Land cover configuration	Effective vegetation cover configuration
CNR	ctr-k5	1993-2019	T255	Climatological (1993-2019)	1993 LC for 1993-2019	k=0.5
	ctr-kv	1993-2019	T255	Climatological (1993-2019)	1993 LC for 1993-2019	k vegetation specific
	pla-k5	1993-2019	T255	Time varying LAI for 1993-2019	1993 LC for 1993-2019	k=0.5
	pla-kv	1993-2019	T255	Time varying LAI for 1993-2019	1993 LC for 1993-2019	k vegetation specific
	plalc-k5	1993-2019	T255	Time varying LAI for 1993-2019	Time varying LC for 1993-2019	k=0.5
	plalc-kv	1993-2019	T255	Time varying LAI for 1993-2019	Time varying LC for 1993-2019	k vegetation specific
MF	ctr	1950-2020	T127	Ecoclimap climatology	2000 LC for 1950-2020	
	pla	1982-2019	T127	Time varying LAI	2000 LC for 1950-2020	
	ila	1950-2020	T127	Dynamic LAI	2000 LC for 1950-2020	
	ila_plc	1950-2020	T127	Dynamic LAI	Time varying LC for 1950-2020 (derived from LUH2)	
ECMWF	ctr	1993-2019	TL639	Climatological (1993-2019)	2019 LC for 1993-2019	
	plc	1993-2019	TL639	Climatological (1993-2019)	Time varying LC for 1993-2019	
	pla	1993-2019	TL639	Time varying LAI for 1993-2019	2019 LC for 1993-2019	
	plalc	1993-2019	TL639	Time varying LAI for 1993-2019	Time varying LC for 1993-2019	

3.4 Evaluation Data and Metrics

Here we describe the reference data used to evaluate the different models. We also describe the evaluation metrics.

3.4.1 Evaporation reference data

The DOLCE (Derived Optimal Linear Combination Evapotranspiration) product combines different global evaporation datasets with in-situ observational data from Fluxnet towers, providing daily evaporation at a 0.25-degree spatial resolution for 1980-2018 (Hobeichi et al., 2021). Here we use the two versions DOLCEv2.1 and DOLCEv3 for evaluation of model evaporation. DOLCEv2.1 is derived from 11 global evaporation datasets and has a smaller bias to flux tower evaporation than DOLCEv3. Therefore, we use DOLCEv2.1 for climatological analyses. DOLCEv3 is a linear combination of evaporation from ERA5-land, GLEAM v3.5a and v3.5b and FLUXCOM-RSMETEO with weights based on flux towers (Hobeichi et al., 2021). DOLCE v3 captures evaporation variations well and is therefore suitable for evaluating the effects of inter-annual varying LAI and LC on model evaporation. In addition, evapotranspiration from FLUXCOM-RSMETEO (combination of FLUXNET, remote sensing and meteorological forcing using machine learning algorithm; Jung et al., 2019) and from CLASS (similar approach to DOLCE but conserving energy balances; Hobeichi et al., 2021) were used as reference datasets for the surface latent heat flux.

3.4.2 Soil moisture reference data

ESA-CCI has developed a global satellite-derived soil moisture product (ESA-CCI SM) based on multiple satellites with active and passive sensors (Dorigo et al., 2017; Gruber et al., 2019). This dataset has a daily temporal resolution for 1978-2019 and is provided at a 0.25-degree grid. Here we used the combined active-passive product interpolated to the model spatial resolution, obtained from https://esa-soilmoisture-cci.org/. The dataset contains spatial and temporal gaps due to densely vegetated areas (tropical forests) and snow coverage. Here we only use grid cells with a temporal coverage larger than 60%. The ESA-CCI SM represents the soil moisture in the top soil layer ~0-5 cm. Here we compare these values to the ECMWF and CNR model first layer soil moisture (7 cm) and the MF model first two layers soil moisture (4 cm). As the represented depths differ, we standardize the SM values using the monthly standard deviation in order to consistently compare the models with the ESA-CCI SM. Another reference data used to evaluate model surface soil moisture (0-10 cm) is the machine learning observationally based soil moisture product SoMo.ml (O and Orth 2021).

3.4.3 Evaluation metrics

Root Mean Square Error

is computed with the following equation:

$$RMSE = \frac{\sqrt{\sum_{t=1}^{T}(\check{y}_t - y_t)^2}}{T}$$

where $\check{y}_t$ and y_t are the absolute model and reference values in time t, respectively, and T is the total considered time steps. For the RMSE of the inter-annual anomalies, the mean seasonal cycles (computed for the bias metric) is removed from the model and reference datasets respectively to obtain the anomalies. Then, the RMSE is estimated based on these anomalies.

Pearson correlation

is computed with the following equation:

$$corr_{x,y} = \frac{cov(X,Y)}{\sigma_x \sigma_y}$$

where *cov* is the covariance, σ_x and σ_y are the standard deviation of X and Y respectively.

Seasonal bias

The mean seasonal cycles (long term mean of every day of the year) for both model and reference datasets are computed. Then the reference's mean seasonal cycle is subtracted from the model's mean seasonal cycle. Finally, the mean bias for each season (DJF-MAM-JJA-SON) is estimated.

4 Results

3.3 Meteo France

The prognostic LAI and the interactive vegetation in SURFEX are evaluated against the CGLS LAI. The impact of the varying LAI on surface latent heat flux is evaluated with offline land surface simulations driven by the ERA5 atmospheric reanalysis. In a second evaluation, two past droughts in Europe are analysed to evaluate the model ability to reproduce LAI anomalies during droughts.

3.3.1 Vegetation modelling

The LAI from ctr is always higher than the CGLS observations (Figure 3). The overestimation of LAI is particularly strong at mid-latitudes in both hemispheres. As shown in Figure 4 in the Northern Hemisphere, there is a particularly strong overestimation of LAI in the boreal forests of Canada and Russia. These overestimations are specific to the Ecoclimap design in which the LAI is estimated by taking the maximum of the envelope of observations on the 1999-2005 period.

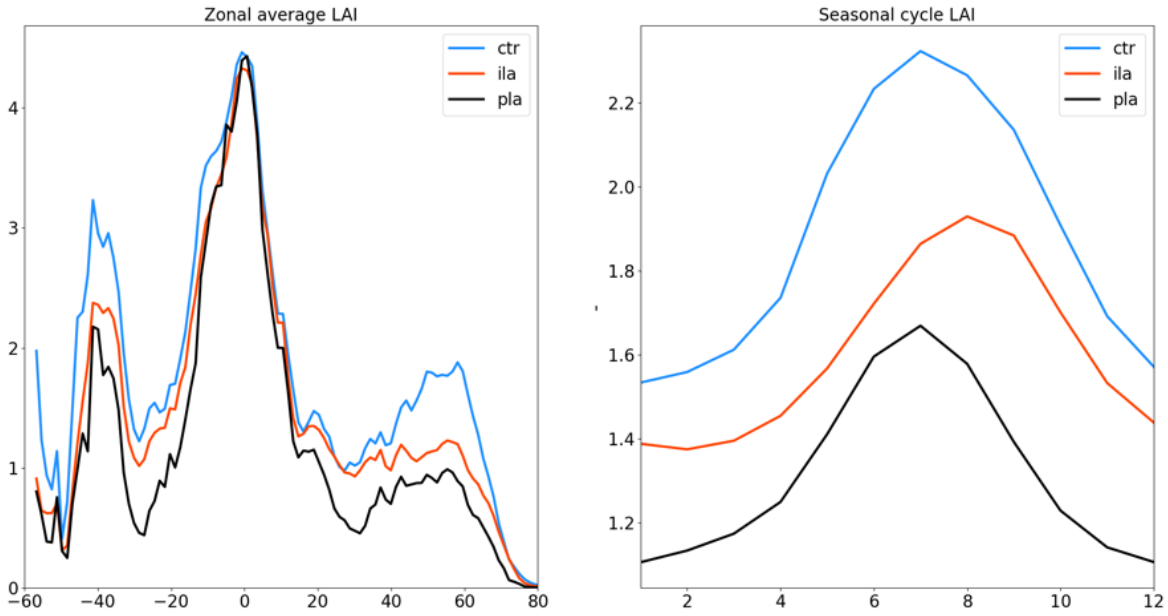

Figure 3 Zonal average (left) and global seasonal cycle (right) of LAI in Ecoclimap (ctr - blue), modelled by the interactive vegetation scheme (ila - red) and in the CGLS LAI (pla - black).

The interactive vegetation scheme also tends to an overestimation of the LAI although strongly reduced compared to ctr. Again, the LAI is overestimated at mid-latitudes of both hemispheres. With the interactive vegetation, the overestimation of LAI is reduced in the boreal forests of North America.

There are persistent overestimations of the LAI in South America and South-East Asia. In the Amazonian Forest, the LAI is underestimated when compared to the observations, because leaf phenology does not depend on the carbon cycle of the leaves only. It is difficult to evaluate the model in this region as a discontinuity has been identified in the observations.

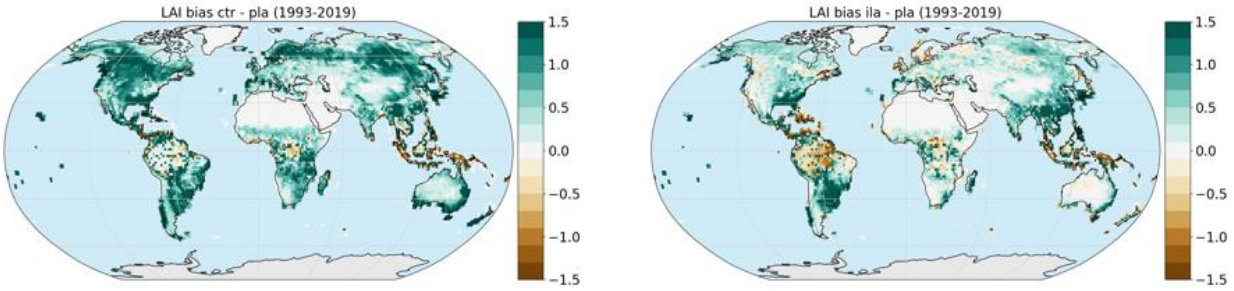

Figure 4 Annual bias of LAI for ctr (left) and the interactive vegetation scheme (ila) (right) against the CGLS LAI for the 1993-2019 period.

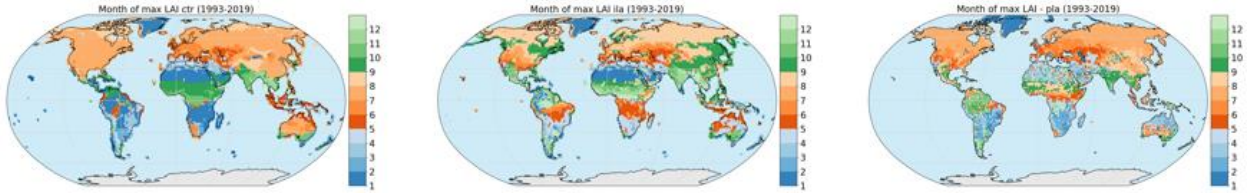

Figure 5 Averaged month on the period 1993-2019 when the maximum LAI occurs in ctr (left), with the interactive vegetation scheme (middle) and in the observations from D1.1 (right) for the 1993-2019 period.

In Figure 5 we observe that the month of maximum LAI in ctr is generally the same as in the observations even if it is patchier in the observations. With the interactive vegetation, there is a shift towards a later maximum of LAI in North America (boreal forest, crops in the USA), Europe (C3 and C4 crops) and Russia. The delay of the seasonal maximum of LAI is a known flaw of the model already documented in Delire et al. (2020) who suggests that it is related to excessive leaf longevity calculated by the model.

It is difficult to draw conclusions about tropical regions as the seasonal cycle is relatively flat in these regions and the month of maximum LAI can vary greatly from one year to the next. In the remaining of the project we will try to better identify and understand the model limitations by looking at the seasonal cycle and its shift by vegetation type

3.3.2 Impacts on surface

In this section, the impacts of the vegetation configuration on the surface latent heat flux are evaluated against DOLCE.

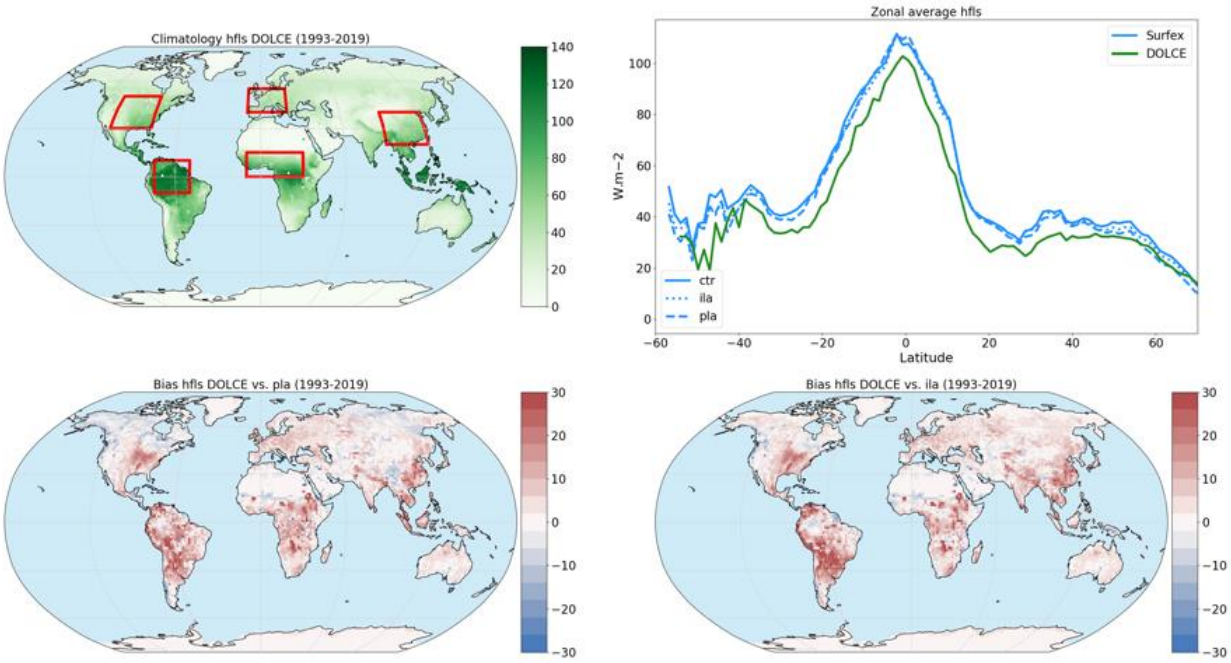

Figure 6 Top left: Climatology of latent heat flux in DOLCE in the period 1993-2019. The red boxes correspond to the regions used in the next figure. Top right: Zonal average of latent heat flux on the period 1993-2019 in DOLCE (green) and in Surfex (blue) in ctr (solid line), with the interactive vegetation scheme (dotted line) and with the prescribed LAI from observations (dashed line). Bottom: Bias of latent heat flux in Surfex with the prescribed LAI from observations (left) and with the interactive vegetation scheme (right) against DOLCE in the period 1993-2019.

The latent heat flux from SURFEX is always stronger, whatever the configuration used. The differences are the strongest in the tropics (South America, Central Africa, South-East Asia). The differences between the configurations of the model are limited, and generally smaller than differences to the reference DOLCE.

However, with a prescribed LAI, the biases on the latent heat flux are reduced in some regions (North America, Sahel, Eastern Asia) even if the global patterns are similar. This suggests the biases on the latent heat fluxes are not coming from the vegetation modelling only.

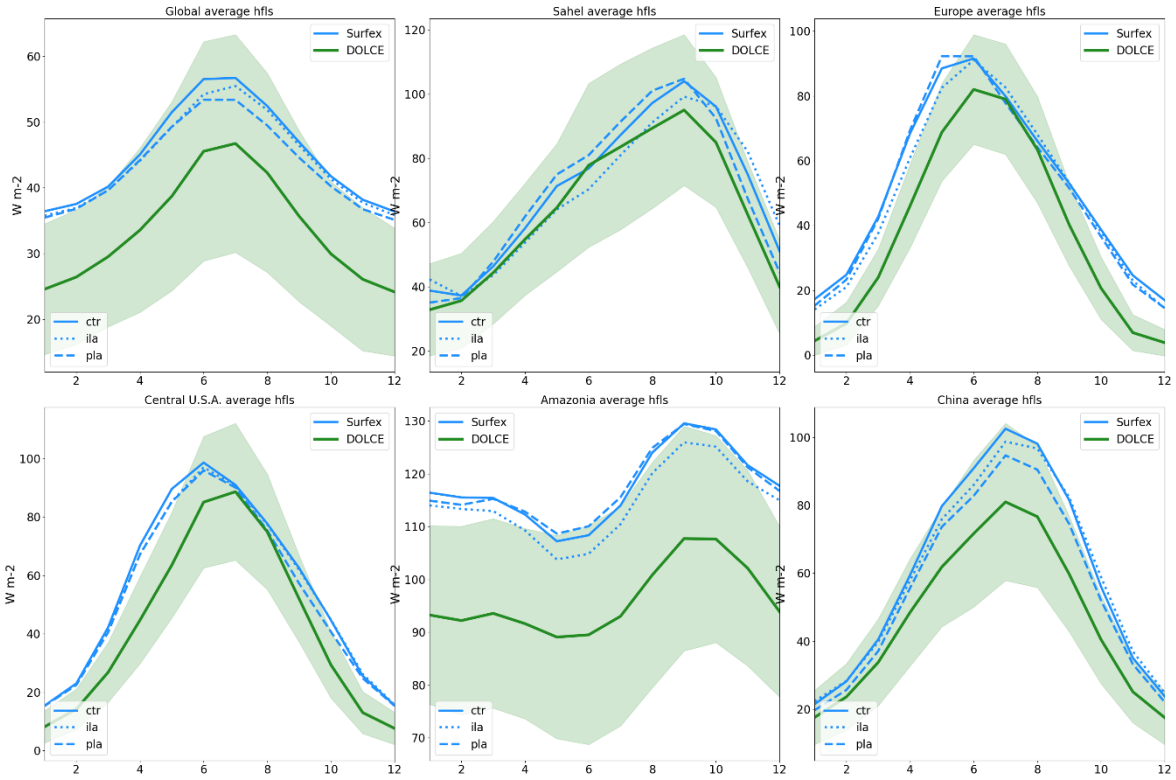

*Figure 7 Seasonal cycle of latent heat flux in DOLCE (green) and in Surfex (blue) with Ecoclimap (solid line), with the interactive vegetation scheme (dotted line) and with the prescribed LAI from observations (dashed line) in the period 1993-2019. The green shading represents the uncertainties (+/- 1.64 * standard deviation) in the estimation of the latent heat flux in DOLCE. Top left is the global average and other regions are defined by the red boxes represented on Figure 6.*

The seasonal cycle of the latent heat flux is evaluated globally and in five regions (Figure 7) for the different vegetation configurations against DOLCE. Consistent with the previous results, the latent heat flux simulated with SURFEX is always stronger than DOLCE, yet generally within the envelope of the observations uncertainties.

In Europe and in the United States, the peak of latent heat flux occurs a month earlier than in DOLCE. In China and the Sahel the seasonal cycle is well correlated with the DOLCE data. The prognostic and prescribed LAI generally lead to a smaller latent heat flux than with the climatological vegetation thus reducing bias. It is expected as the LAI is smaller in these configurations.

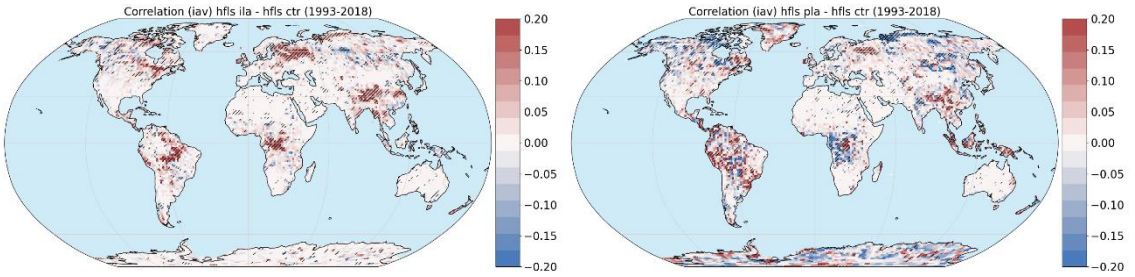

Figure 8 Correlation difference of inter-annual anomaly latent heat with respect to DOLCE between Surfex with the interactive vegetation scheme and Ecoclimap (left) and with the prescribed LAI from observations and Ecoclimap (right) for the period 1993-2019.

The prognostic LAI improves correlation in some regions (South America and Africa tropical forests) without deteriorating the results. Results are more mixed with the prescribed LAI which shows very limited improvements and even tends to deteriorate results in some regions (Northern Canada, eastern Russia). In the tropics, the CGLS LAI shows spurious trends and it is therefore difficult to draw conclusions on the impacts of LAI on the latent heat flux in these regions.

3.3.3 Droughts and interactive vegetation

The vegetation state can have a significant impact during extreme events and particularly during droughts. The impact of the interactive vegetation scheme is evaluated during the European and Russian heat waves of 2003 and 2010.

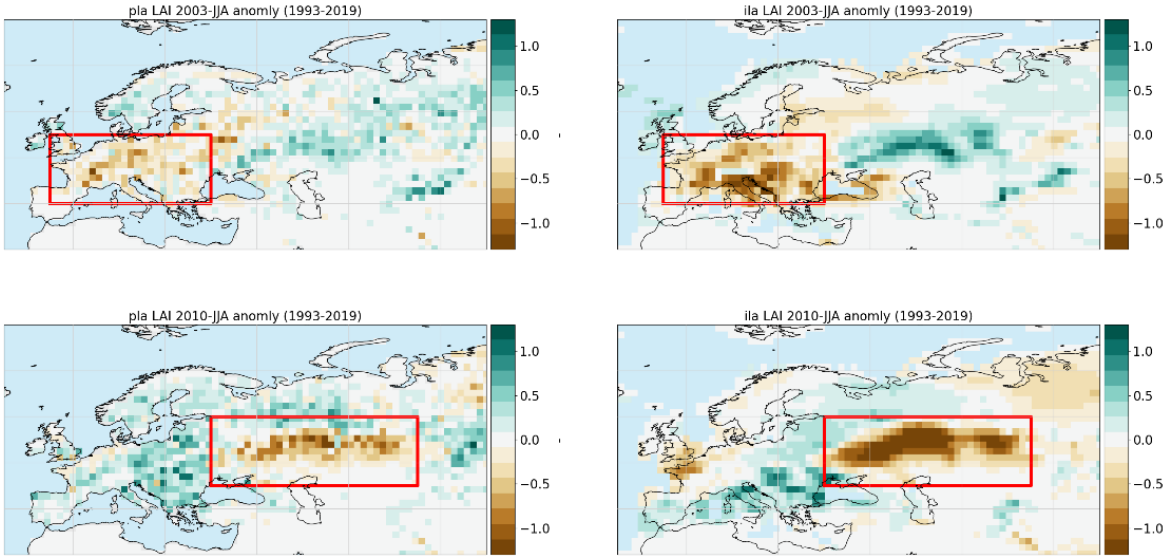

Figure 9 2003 (top) and 2010 (bottom) summer (JJA) anomalies of LAI in the CGLS observations (pla - left) and in Surfex with the interactive vegetation scheme (ila - right). The reference period is 1993-2019.

The anomalies of LAI simulated in 2003 and 2010 with SURFEX are larger than in the CGLS observations. However, the locations of the anomalies are correct, particularly in 2010.

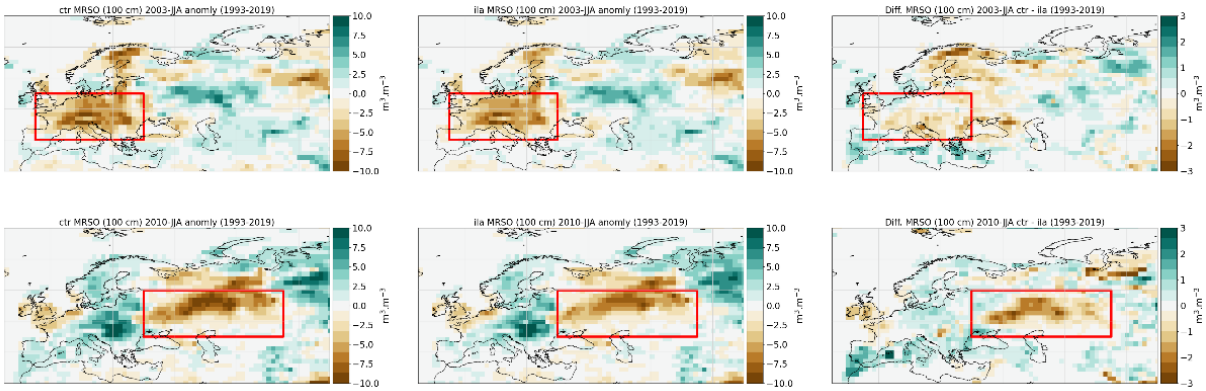

Figure 10 2003 (top) and 2010 (bottom) summer (JJA) anomalies of 100 cm soil moisture Surfex with Ecoclimap (ctr - left) and with the interactive vegetation scheme (ila - middle) and the differences between the two configurations (right). Note the different scale for the differences. The reference period is 1993-2019.

In the cases studied, soil moisture anomalies are lower (less negative) with the interactive vegetation than in ctr. It might be related to the stronger LAI anomalies that lead to a smaller evapotranspiration and therefore a smaller draining of the soil. The interactive vegetation tends to mitigate the negative anomalies of soil moisture.

3.4 ECMWF

The evaluation of the impact of the varying LAI and LULC data on the offline surface simulations is performed with two main focuses. The first is to check the model skills with regards to long term mean metrics on the surface latent heat flux and surface soil moisture (0-10 cm). The model skill is evaluated for representing the three variables after model updates with the land use dataset from ESA-CCI and in the inter-annual variability of LAI and cover fraction. The second evaluation focuses on the ability of the model to detect extreme events such as droughts when forced with varying vegetation related data.

3.4.1 Long term mean sensitivity and evaluation

Evapotranspiration from FLUXCOM (Jung et al., 2019) is used as reference observationally based dataset for the surface latent heat flux. The machine learning observationally based soil moisture product SoMo.ml (O and Orth 2021) is used as the reference dataset to evaluate model surface soil moisture (Section 3.4.2). In this long term mean model evaluation, the global land area with a daily temporal resolution at 0.5x0.5 degrees spatial resolution is considered.

For all experiments listed in Table 1 and for the three variables of interest, the model skill is evaluated. For the surface latent heat flux, the following model skill metrics are used (Section 3.4.3): bias and RMSE. For the surface and deep soil moisture the Pearson correlation is used.

Surface latent heat flux

Figure 11 to Figure 14 show the model skill metrics of the surface latent heat flux for the different simulation configurations. The comparison against FLUXCOM dataset with the bias and anomaly RMSE metrics is depicted. For the control simulation (Figure 11), large biases in the Northern and Southern hemisphere during JJA and DJF, respectively (i.e. their respective summer season) are generally seen. Specifically, we see a strong positive bias over Northeastern North America and Eurasia. North eastern South America shows generally negative biases all year round, especially in JJA. Southern Africa shows large positive (negative) bias during DJF (JJA).

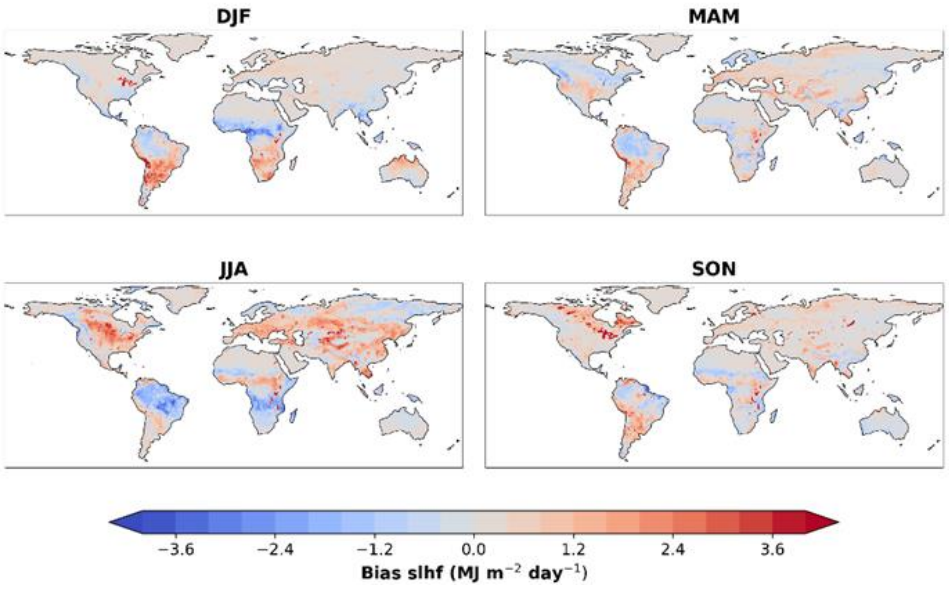

Figure 11 Bias in latent heat flux in the CTR simulation

In Figure 12 to Figure 14 the differences of the varying vegetation related model configurations experiments with regards to the CTR (control) simulation are illustrated. Red (blue) color indicates a less (more) accurate surface latent heat flux of the considered model configuration with regards to the control experiment based on the FLUXCOM product. While the model shows a slight improvement with regards to the FLUXCOM data when using only varying LULC data (PLC) (Figure 12), a pronounced deterioration with regards to the control experiment (Figure 13 and Figure 14) is depicted when using the time varying LAI (PLA and PLALC experiments). This indicates that time-varying LAI has a stronger effect on the modulation of the latent heat flux in ECLand, than time-varying LULC

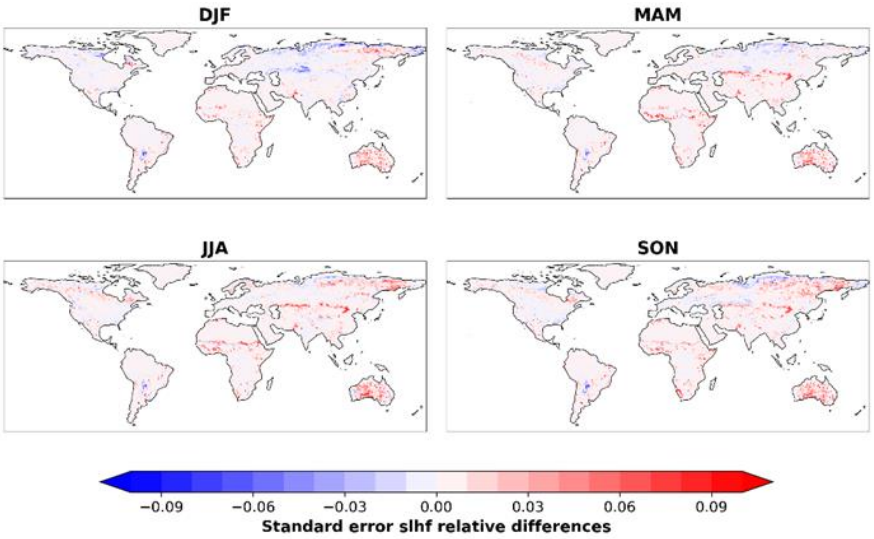

Figure 12 Relative differences in RMSE in latent heat flux anomalies between PLC and CTR simulations

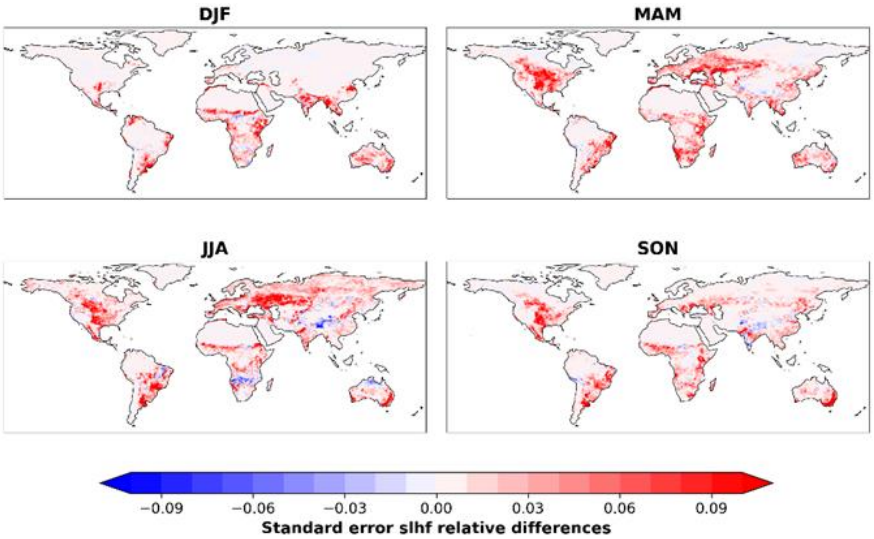

Figure 13 Relative differences in RMSE in latent heat flux anomalies between PLA and CTR simulations

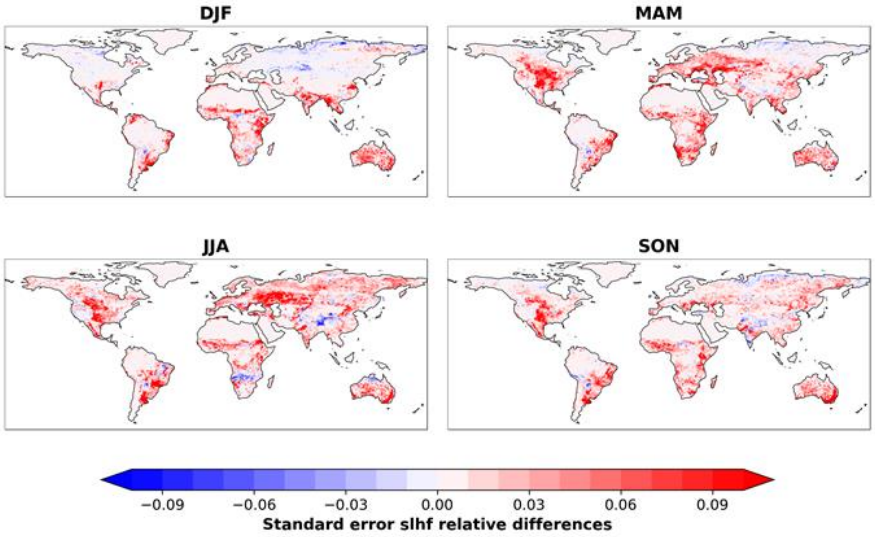

Figure 14 Relative differences in RMSE in latent heat flux anomalies between PLALC and CTR simulations

Soil Moisture

Figure 15 to Figure 18 show the model skill metric for the surface soil moisture against SoMo.ml products for the different simulation configurations. Figure 15 illustrates the correlation of the control simulation surface soil moisture with the SoMo.ml surface soil moisture data for all seasons. The strong positive correlation indicates that the model control configuration has already good skill in capturing the spatial and seasonal variability of the surface soil moisture. Only the Northernmost regions of the Northern hemisphere during DJF and MAM show slightly negative correlation, probably due to the model's difficulties in representing very cold and freezing soil temperatures.

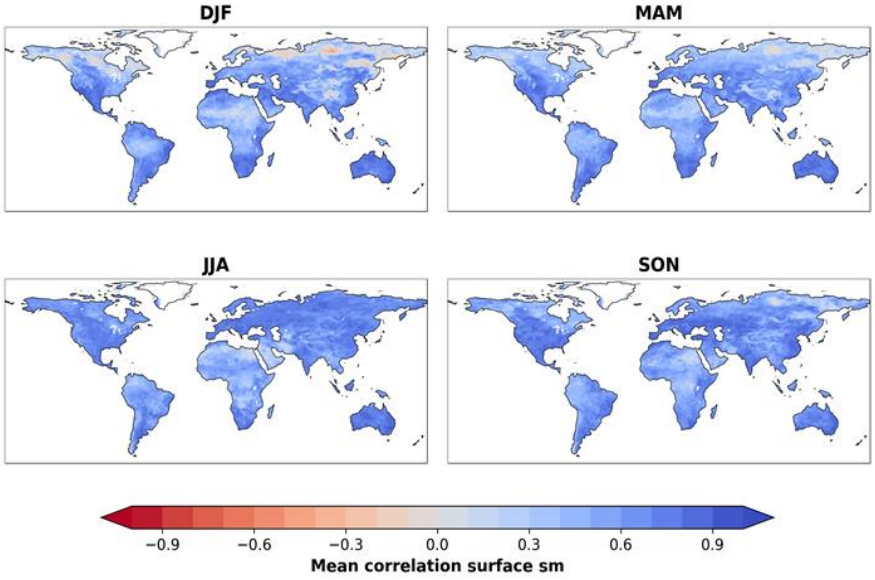

Figure 15 Pearson correlation between SoMo.ml and ECLand surface soil moisture in the CTR simulation

Figure 16 to Figure 18 show the differences of the correlation with regards to the SoMo.ml data of the varying vegetation-related model configurations experiments from the CTR (control) simulation. Unlike the surface latent heat flux results, the surface soil moisture from the varying LULC (PLC, Figure 16) shows regions with better skills (blue color) than the control experiment. These regions are mostly

located in the Northern hemisphere, in regions where skill is the lowest in the CTR simulation. When introducing the varying LAI (PLA, Figure 17) and (PLALC, Figure 18) model deterioration (red colors) appears mainly in dry and arid areas but also in areas characterized by crops and low vegetation. Similar to the surface latent heat flux results, the experiments with time varying LAI show larger differences with regards to the control experiment (Figure 17 and Figure 18) than the experiment with time varying LULC only (Figure 16).

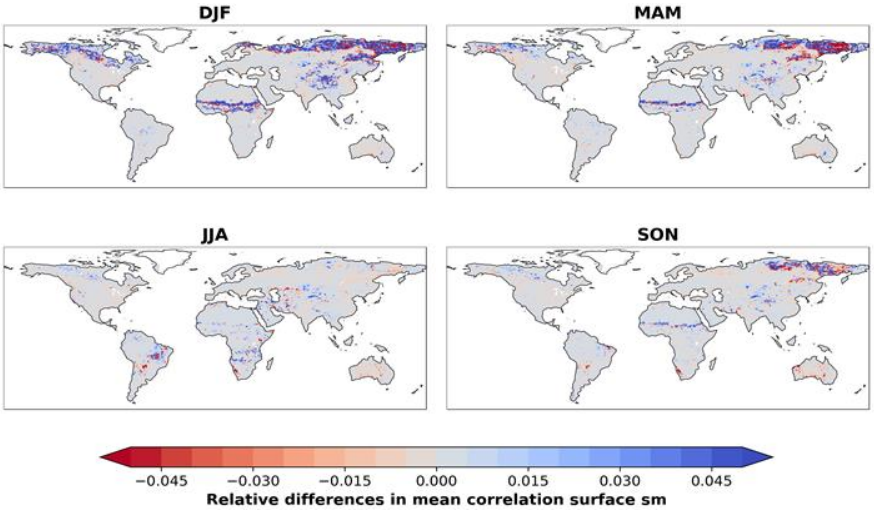

Figure 16 Relative differences in mean correlation of surface soil moisture anomalies between PLC and CTR simulations

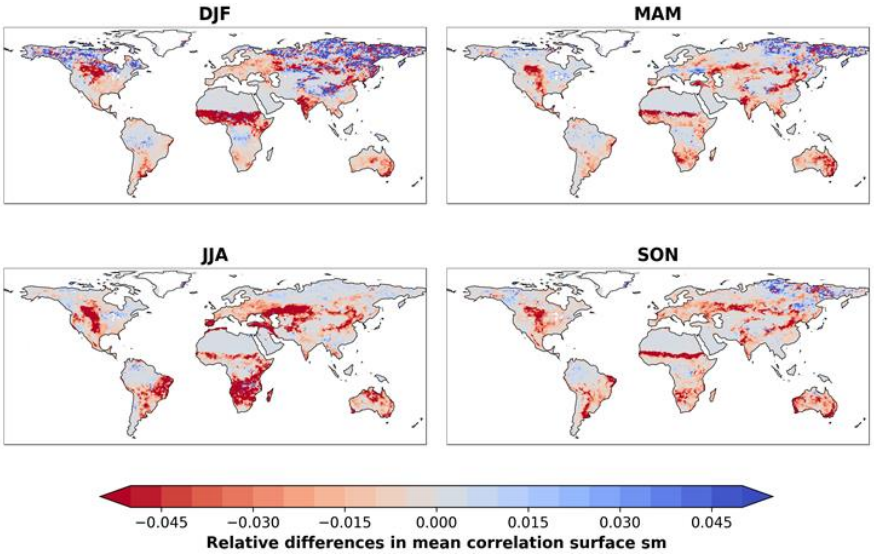

Figure 17 Relative differences in mean correlation of surface soil moisture anomalies between PLA and CTR simulations

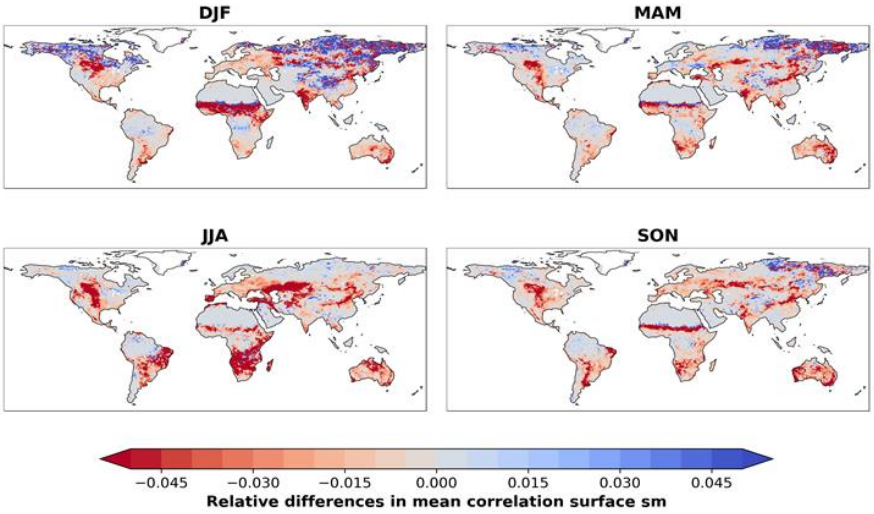

Figure 18 Relative differences in mean correlation of surface soil moisture anomalies between PLALC and CTR simulations

The above results emphasize the need for a better estimation of the land surface parameters given that they were adapted to previous data set and tuned to improve atmospheric processes and skill for operational numerical weather prediction. To note that besides the time varying change for LAI, the way these data are disaggregated into high and low vegetation components was also revised (D1.1) and this change combined with the new LULC maps has a strong impact on the model climate state.

3.4.2 Extreme cases evaluation

The vegetation state can have a prominent influence on the global energy, water and carbon cycles, up to seasonal and decadal time scales. This has been particularly evident during extreme conditions in recent years (e.g. Europe 2018 and 2003 droughts, United State 2011 drought, Russia 2010 heat wave, Horn of Africa 2010 drought..). Weather parameters are also sensitive to the land use/land cover and vegetation state and particularly to LAI that contribute to the partitioning of the surface energy fluxes into latent and sensible fluxes, and the development of planetary boundary conditions and clouds.

The impact of using varying LAI and LULC is evaluated in this section by focusing on extreme events. We examine the surface fluxes derived from ECLand offline simulations performed at the global scale for the period covering (1993 to 2019). However, the results are focused on 2003 and 2010 because they contain an extreme drought event over Europe and a heat wave over Russia.

Focusing on the 2010 extremes events, during the July 2010 Russian heat waves, the LAI was lower than the 10th percentile of the whole 1993–2019 period. In the case of the European 2003 drought, the LAI was much lower than the 10th percentile (see following sections and D1.1).

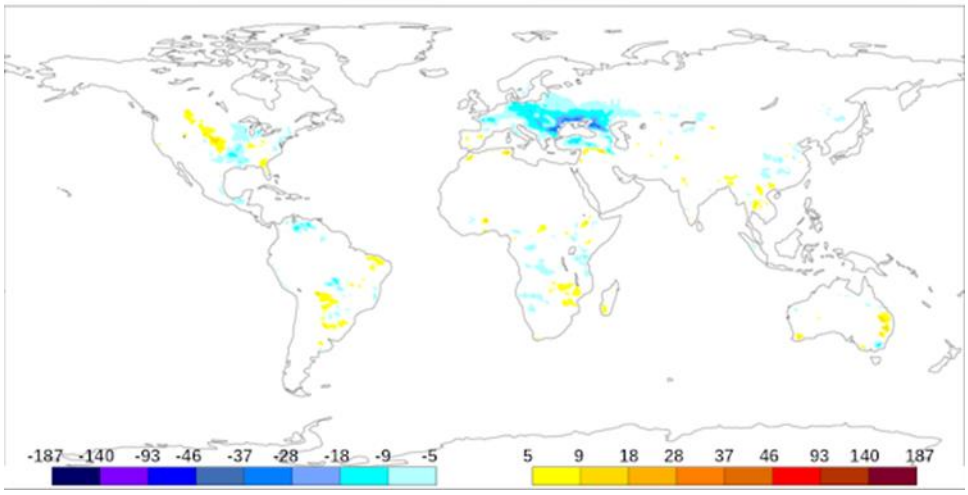

Figure 19 Latent Heat flux difference (W/m2) between time varying LAI and LULC and control simulation (PLALC - CTR) for the European drought (April 2003).

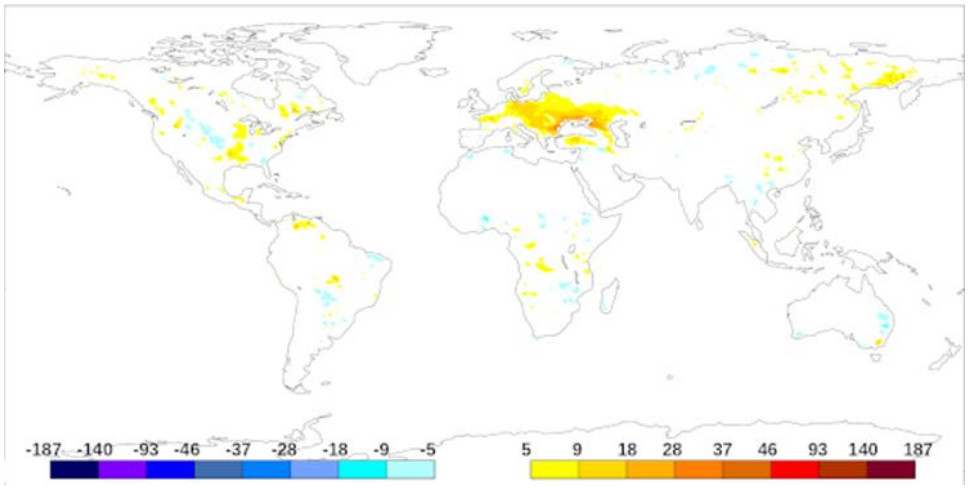

Figure 20 Sensible Heat flux difference (W/m2) between time varying LAI and LULC and control simulation (PLALC - CTL) for the European drought (April 2003).

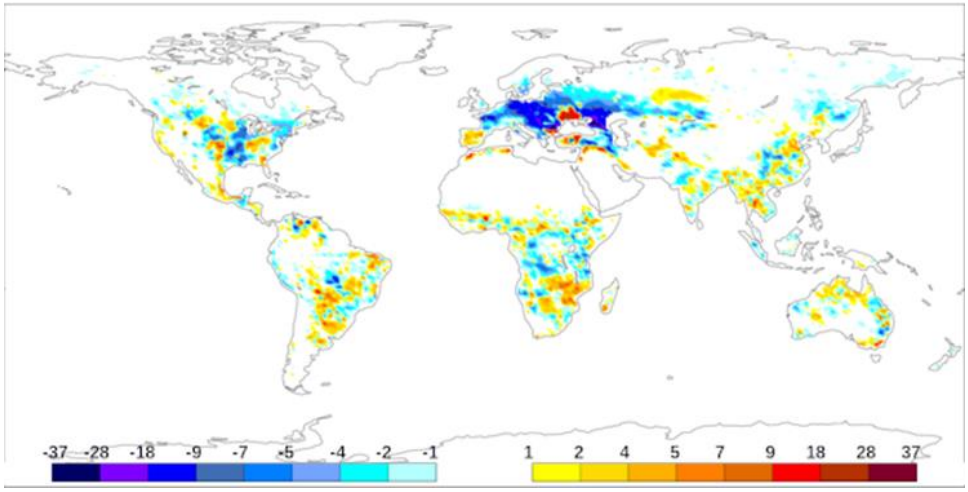

Figure 21 Latent Heat flux bias difference with regards to CLASS data(W/m2) between time varying LAI and LULC and control simulation (PLALC - CTR) for the European drought (April 2003)

As a consequence of the observed decrease of LAI over Europe in 2003 and Russia in 2010, a decrease in the Latent heat flux (Figure 19) and an increase in the sensible heat flux (Figure 20) resulted from the model for both PLA and PLALC configurations (only the PLALC case is shown for illustration). When using the inter annual varying vegetation data, the reduction in energy fluxes reached in some areas 30W/m2, while the model bias with regards to the CLASS observationally based data (Hobeichi et al. 2020) was reduced by up to 20W/m2. Similar to the results of the long term means evaluation, the experiment using only varying LULC (PLC) showed a minor impact on both latent and sensible heat fluxes related to a mild increase of the surface albedo (not shown) which induces a decrease in the net surface radiation. However, when varying LAI and LULC (PLALC) are combined, the resultant anomaly signal of both latent and sensible heat fluxes is mainly driven by the LAI anomaly.

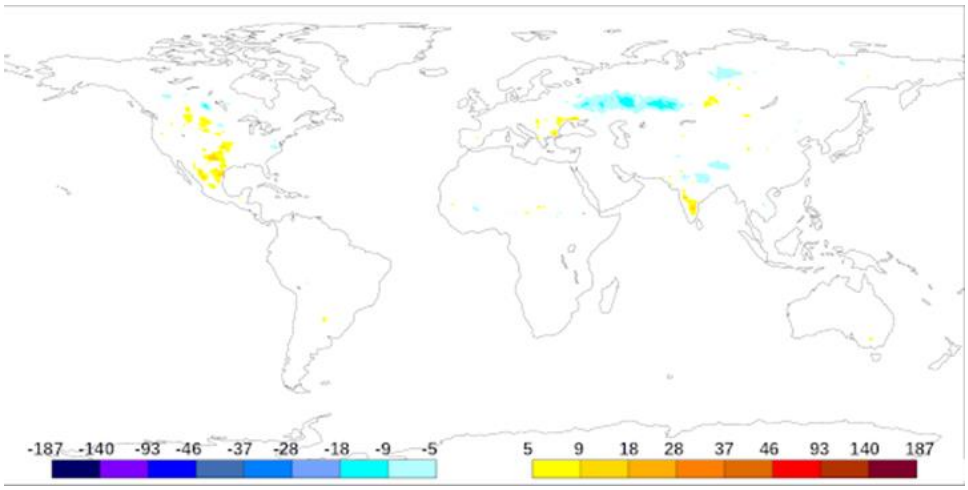

Figure 22 Latent Heat flux difference (W/m2) between time varying LAI and LULC and control simulation (PLALC - CTR) for the Russian heatwave (July 2010).

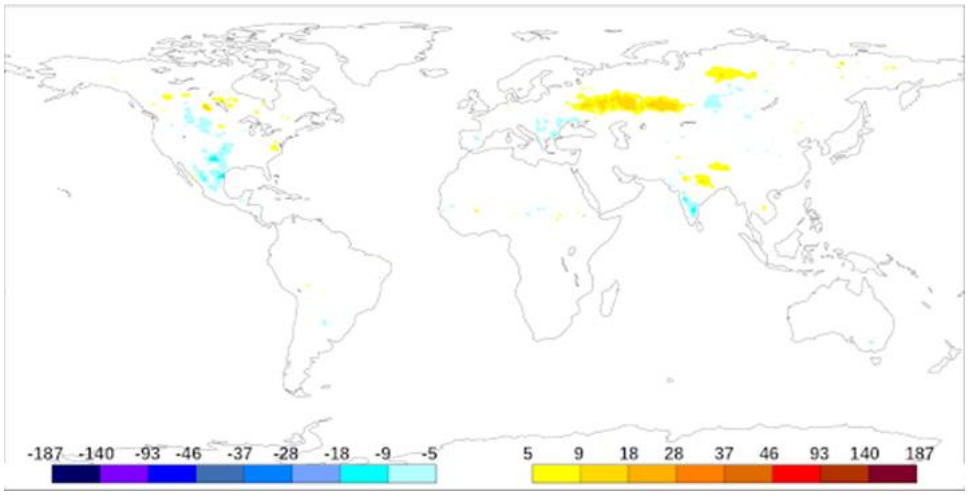

Figure 23 Sensible Heat flux difference (W/m2) between time varying LAI and LULC and control simulation (PLALC - CTR) for the Russian heatwave (July 2010).

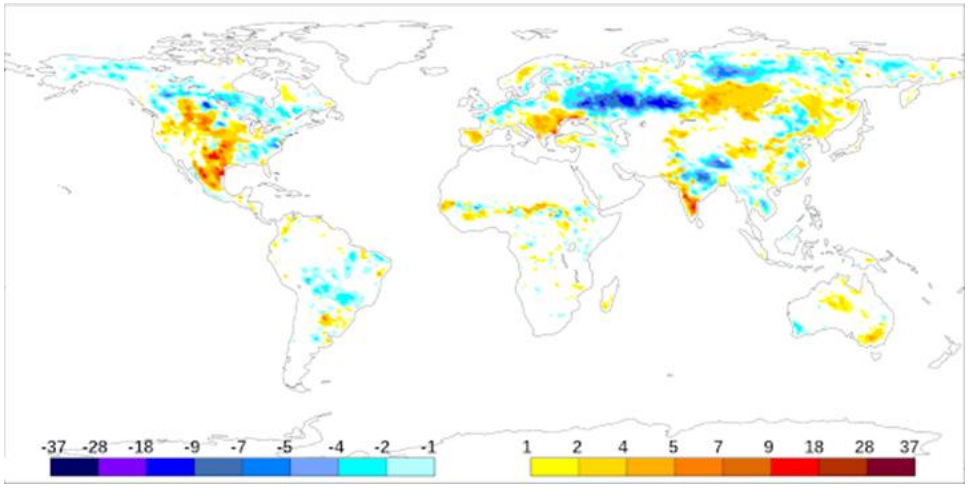

Figure 24 Latent Heat flux bias difference with regards to CLASS data (W/m2) between time varying LAI and LULC and control simulation (PLALC - CTR) for the Russian heatwave case (July 2010)

For the Russian 2010 heat wave case, similar results are obtained. The energy fluxes difference during July 2010 over Russia when using the prescribed varying vegetation data PLALC was up to 18W/m2 (Figure 22 and Figure 23) and this contributed to reducing the bias by up to 18 W/m2 (Figure 24).

3.5 CNR

3.5.1 Vegetation variability representation

Inter-annual variability LAI and land cover

The monthly CGLS LAI represents the inter-annual variations in LAI. The data shows the largest anomaly variations in semi-arid regions where vegetation transpiration is water limited (North-East Brazil, Pampas and South-East Australia) (Figure 25a) and during summer months when LAI is high (Figure 25b and c). Dry and wet years can be distinguished by the data as negative and positive anomalies, respectively.

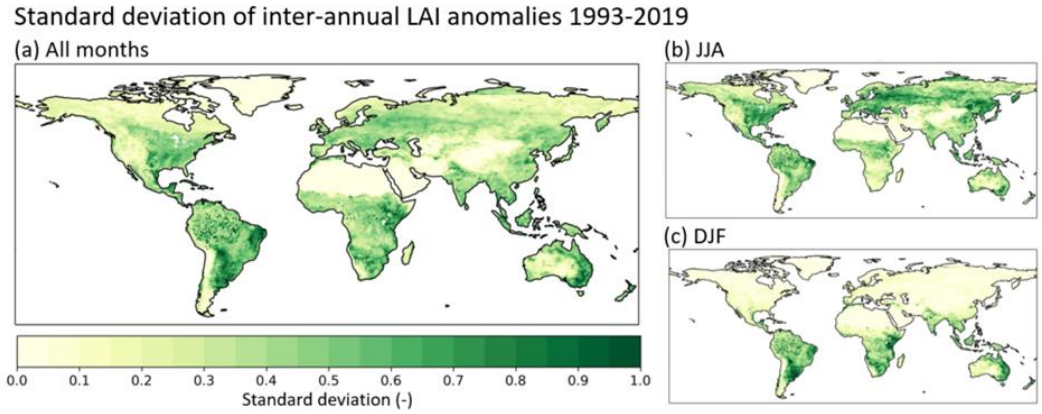

Figure 25 Standard deviation of inter-annual LAI anomaly introduced in the model in 1993-2019 for (a) all months, (b) JJA and (c) DJF.

The standard deviation of LAI inter-annual anomalies over the tropics (-15 < latitude < +15) is on average 0.33 for the 1993-2019 period. However, the standard deviation over the tropics for the 1999-2019 period is 0.22, which is considerably smaller (Figure 26a). Figure 26b shows that there is a shift in the LAI between the 1993-1999 and 1999-2019 period over the tropics, in other regions we did not find similar effects. This is likely due to limitations of the CDF-matching approach that was used for the harmonization of the AVHRR (1993-1999) and CGLS (1999-onwards) data (CONFESS D1-1). As LAI strongly controls the model evaporation, interpretation of the modelling results over the tropics should be done with care.

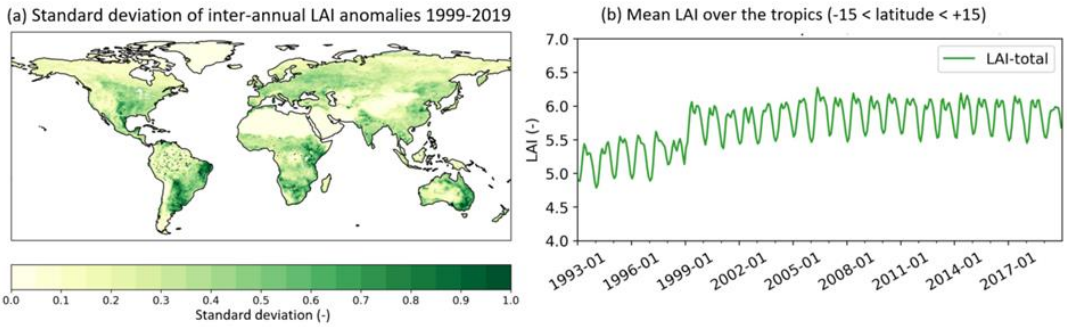

Figure 26 (a) Standard deviation of inter-annual LAI anomaly introduced in the model in 1999-2019 for all months and (b) timeseries of mean LAI over the tropics (-15 < latitude <+15).

With the ESA-CCI land cover data, the dominant vegetation types change in only 6% of the HTESSEL land grid cells over the period 1993-2019 (Figure 27a, b, c, d). This small effect is partially a

consequence of the HTESSEL representation of dominant vegetation type that does not allow for mixed vegetation types or representation of subgrid variability.

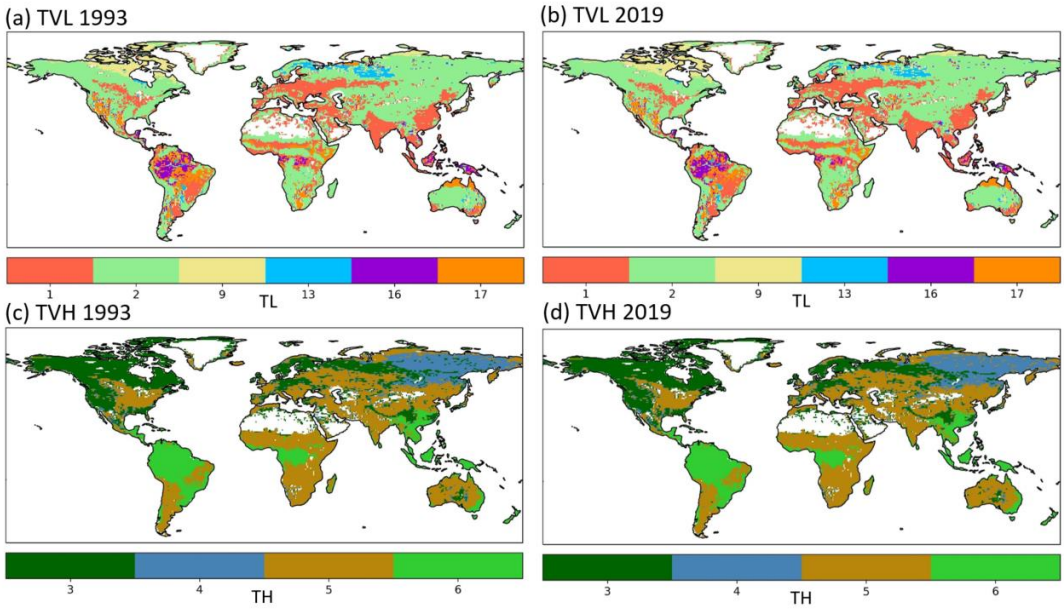

Figure 27 Model low (TL) (a,b) and high (TH) (c,d) vegetation types for the years 1993 and 2019. Vegetation indices in Table 1.

On the other hand, the vegetation fractional coverage changes in many regions with the ESA-CCI land cover dataset. Low vegetation replaces high vegetation due to deforestation in for example the Amazon (point 1 in Figure 28c, d) and Siberia (point 3 in Figure 28c, d). In arid regions (e.g. central Asia and Australia (point 4)) we observe an expansion of low vegetation (Figure 28c), while in the boreal forests high vegetation increases (point 2 in Fig. Figure 28d).

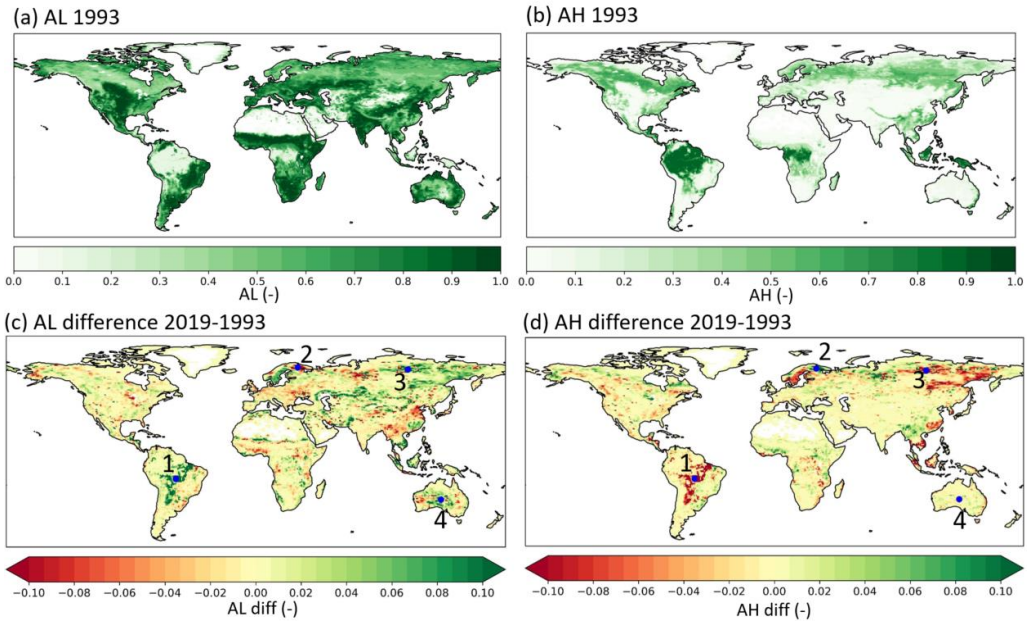

Figure 28 Model low (AL) and high (AH) vegetation fractional cover in 1993 (a, b) and difference between 2019 and 1993 AL (c) and AH (d).

Improved effective vegetation cover parameterization

Figure 29 shows that the optimized LAI-FCover relation has smaller k than in the control case of k=0.5 for all vegetation types. The k values for low vegetation types are higher than for high vegetation types, except for tundra. The presented data points in Figure 29 cover the entire LAI-range, except for the tundra where LAI does not exceed a value of 2. However, the density of data points is not well spread, with for example mostly LAI between 0 and 1 for crops and LAI between 5 and 7 for evergreen broadleaf forests.

The effective vegetation cover with the new parameterization reduces RMSE with respect to the FCOVER data compared to the k=0.5 model setup (Figure 30). The RMSE reduces the most over the boreal and tropical forests in kv compared to k5 for all seasons, with for evergreen needleleaf trees an average RMSE reduction from 0.116 to 0.064 and for evergreen broadleaf trees from 0.054 to 0.032. The differences in regions with predominantly low vegetation are smaller because the fitted k-value is closer to the original k=0.5 (e.g. crops from 0.061 to 0.054 and short grass from 0.041 to 0.038).

The RMSE patterns are similar for different seasons (Figure 30b and c), except for high latitudes with predominantly low vegetation cover (JJA Canada and North-East Russia). Here tundra and short grass vegetation cover are dominant and the JJA RMSE increases from 0.018 in k5 to 0.036 in kv.

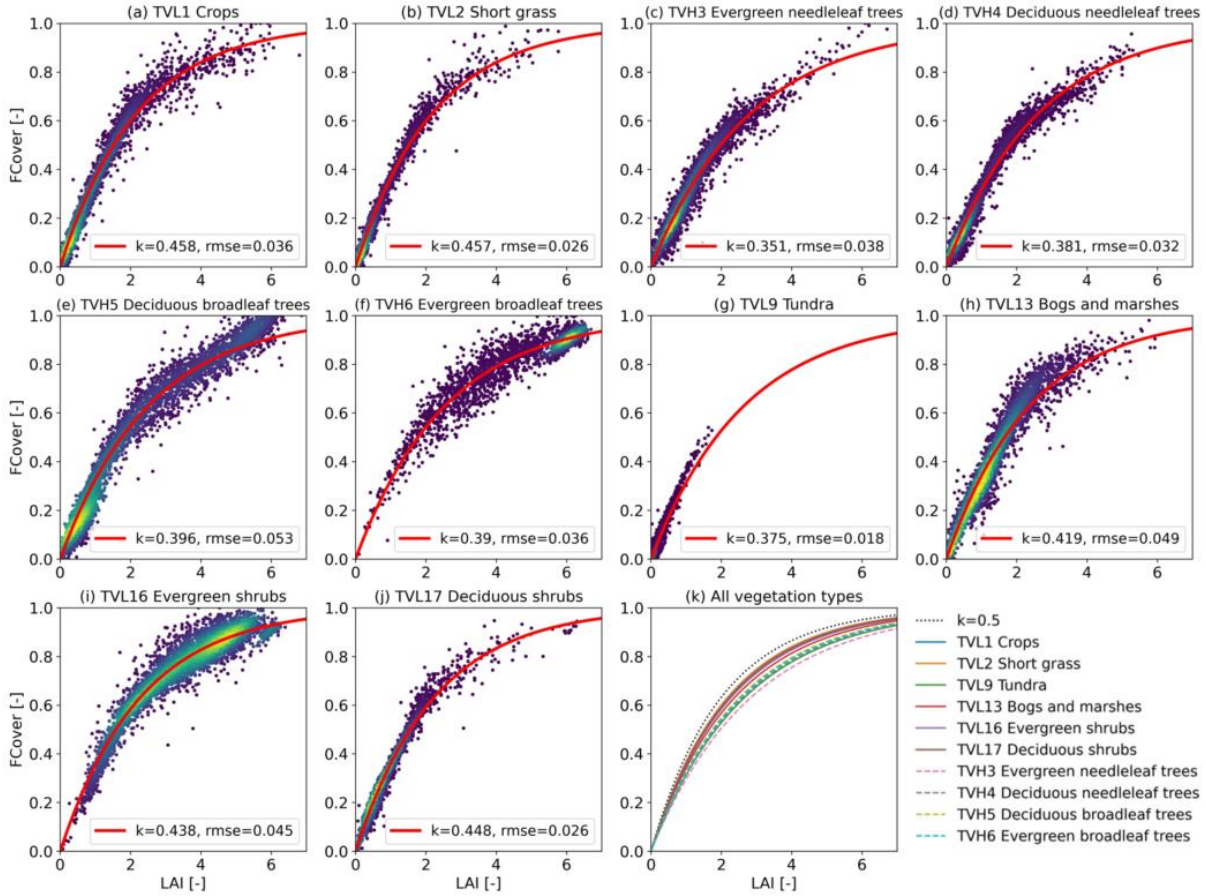

*Figure 29 (a – j) LAI vs FCover for a subsample (5000) of the selected points (section 3.2.3) for the least squares optimization for all vegetation types and the fitted curve. The colors indicate the point density with purple a low density and yellow a high density, k-values and RMSE of the fit are given in the legend (k) The new effective cover parameterization for all vegetation types together FCover = 1-exp(-k*LAI)*

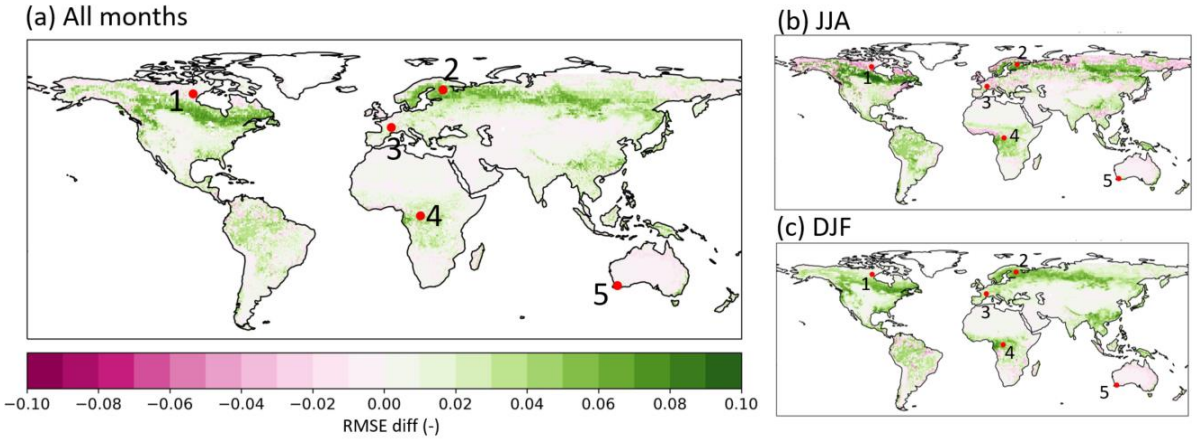

Figure 30 (a) RMSE difference of model effective cover (CVL+CVH) vs FCOVER data between K5 and KV for 1999-2019 for (a) all months (b) DJF and (c) JJA. The five points are highlighted for timeseries in Figure 32.

3.5.2 Impacts on surface fluxes

Vegetation variability

The effects of the inter-annual varying LAI from CGLS on model surface fluxes are discussed in the multi-model evaluation in Section 4.4 - Multi model comparison.

Figure 31 and Table 4 show the effect of the variability in land cover on model evaporation fluxes in four specific points from Figure 28. The variability in land cover by implementing ESA-CCI annual land cover data (plalc) results in an increased variability in model evaporation compared to the fixed land cover (pla) and a shift in the individual evaporation fluxes (Et: transpiration, Es: soil evaporation and Ei: interception evaporation). For the Brazil deforestation case (1) the mean model Et reduces from 1.808 to 1.700 mm/day and Ei reduces from 0.937 to 0.836 mm/day. This reduction goes together with an increase in Es from 0.481 to 0.599 mm/day, because low vegetation has a smaller effective vegetation cover fraction than high vegetation and thus a larger bare soil fraction where soil evaporation occurs. In the Brazil case (1) the total evaporation reduces, while for the Russia deforestation (case 3) E slightly increases due to the relatively large contribution of soil evaporation to total evaporation. On the other hand, the increase in high vegetation (Finland (2)) and the expansion of low vegetation (Australia (4)) lead to small increases in model, as a result of an increase of Et and Ei and a reduction of Es.

The limited effects of varying land cover on model evaporation are partly caused by the coupling with the CGLS LAI. The LAI was disaggregated into high and low LAI based on the ESA-CCI varying land cover data (D1-1), so the changes in land cover are partly included in the CGLS LAI which was used in both experiments here.

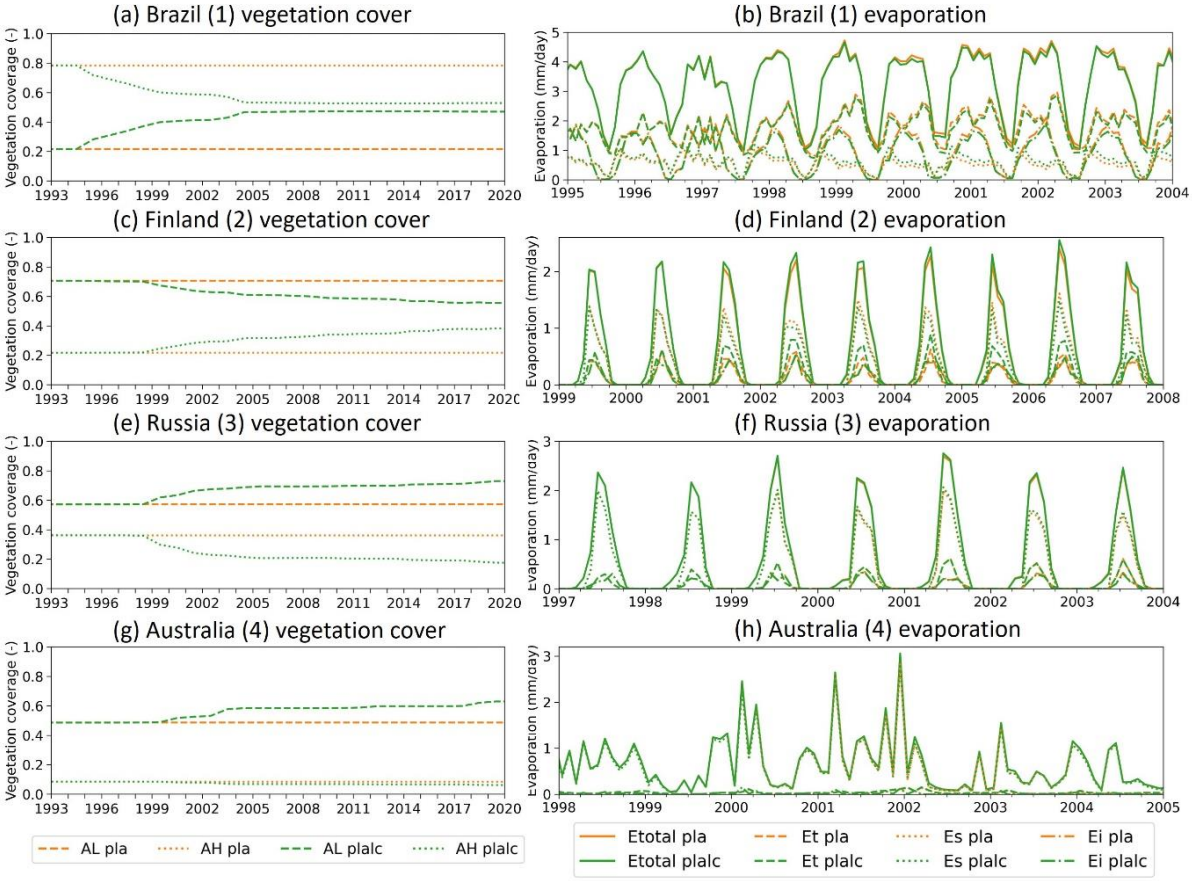

Figure 31 Timeseries for the four specific points pointed in the maps in Figure 28 of vegetation cover AH and AL (a, c, e, g) and (b, d, f, h) model evaporation with E total evaporation, Et transpiration, Es soil evaporation and Ei interception evaporation in pla and plalc.

Table 4 Mean and standard deviation of model E, Et, Es and Ei fluxes for experiment pla and plalc for the four points from Figure 28. All values are in mm/day.

Point in Figure 28	Experiment	Mean E	Mean Et	Mean Es	Mean Ei	Std E	Std Et	Std Es	Std Ei
1 Brazil	pla	3.225	1.808	0.481	0.937	1.161	0.536	0.243	0.698
	plalc	3.146	1.700	0.599	0.846	1.167	0.539	0.303	0.630
2 Finland	pla	0.548	0.105	0.330	0.109	0.761	0.171	0.458	0.153
	plalc	0.574	0.144	0.309	0.114	0.796	0.238	0.427	0.162
3 Russia	pla	0.584	0.089	0.396	0.059	0.835	0.167	0.608	0.095
	plalc	0.585	0.081	0.412	0.054	0.843	0.151	0.634	0.088
4 Australia	pla	0.543	0.027	0.503	0.013	0.547	0.028	0.516	0.021
	plalc	0.544	0.030	0.499	0.014	0.547	0.031	0.513	0.022

Effective vegetation cover

The effective vegetation cover controls the evapotranspiration-flux components (Et, Es and Ei) differently. A decrease in effective vegetation cover results in an increase of the bare soil fraction and consequently an increase of model Es. With smaller effective high and low vegetation fractions, model Et and Ei reduce.

In Finland (case 2; boreal forest) and Central Africa (case4; tropical forest) the effective vegetation fraction consistently reduces and is closer to the FCOVER data (Figure 32a). For these points a clear, yet mild, shift in internal evaporation fluxes is observed, with on average Es increasing, Et and Ei decreasing (Table 5). Similarly, the variability in Et and Ei decrease with the reduction in model effective cover (Table 5). Although the evaporation partitioning is affected by the new effective cover parameterization, the total evaporation (mean and variability) does not considerably change (Figure 32b; Table 5). The limited effects are partially related to the small difference in parameter k (Figure 29) compared to the control case (k=0.5). Moreover, we hypothesize that the limited effects on total evaporation are controlled by the fixed atmospheric moisture demand in the offline model setup.

Table 5 Mean and standard deviation of model E, Et, Es and Ei fluxes for experiment plalc-k5 and plalc-kv for the five points from Figure 30. All values are in mm/day

Point in Figure 30 Figure 28	**Experiment**	**Mean E**	**Mean Et**	**Mean Es**	**Mean Ei**	**Std E**	**Std Et**	**Std Es**	**Std Ei**
1 Canada	k5	0.625	0.080	0.409	0.052	0.777	0.143	0.592	0.088
	kv	0.626	0.073	0.421	0.047	0.778	0.131	0.610	0.081
2 Finland	k5	0.817	0.326	0.293	0.177	1.019	0.487	0.367	0.230
	kv	0.816	0.286	0.356	0.158	1.034	0.431	0.451	0.208
3 France	k5	1.923	1.067	0.465	0.392	1.312	0.947	0.270	0.241
	kv	1.914	1.021	0.516	0.377	1.308	0.914	0.300	0.236
4 Central Africa	k5	3.796	2.367	0.376	1.053	0.373	0.341	0.097	0.396
	kv	3.771	2.250	0.511	1.010	0.375	0.321	0.122	0.382
5 Australia	k5	0.986	0.211	0.672	0.103	0.554	0.284	0.349	0.102
	kv	0.986	0.199	0.689	0.098	0.553	0.269	0.355	0.098

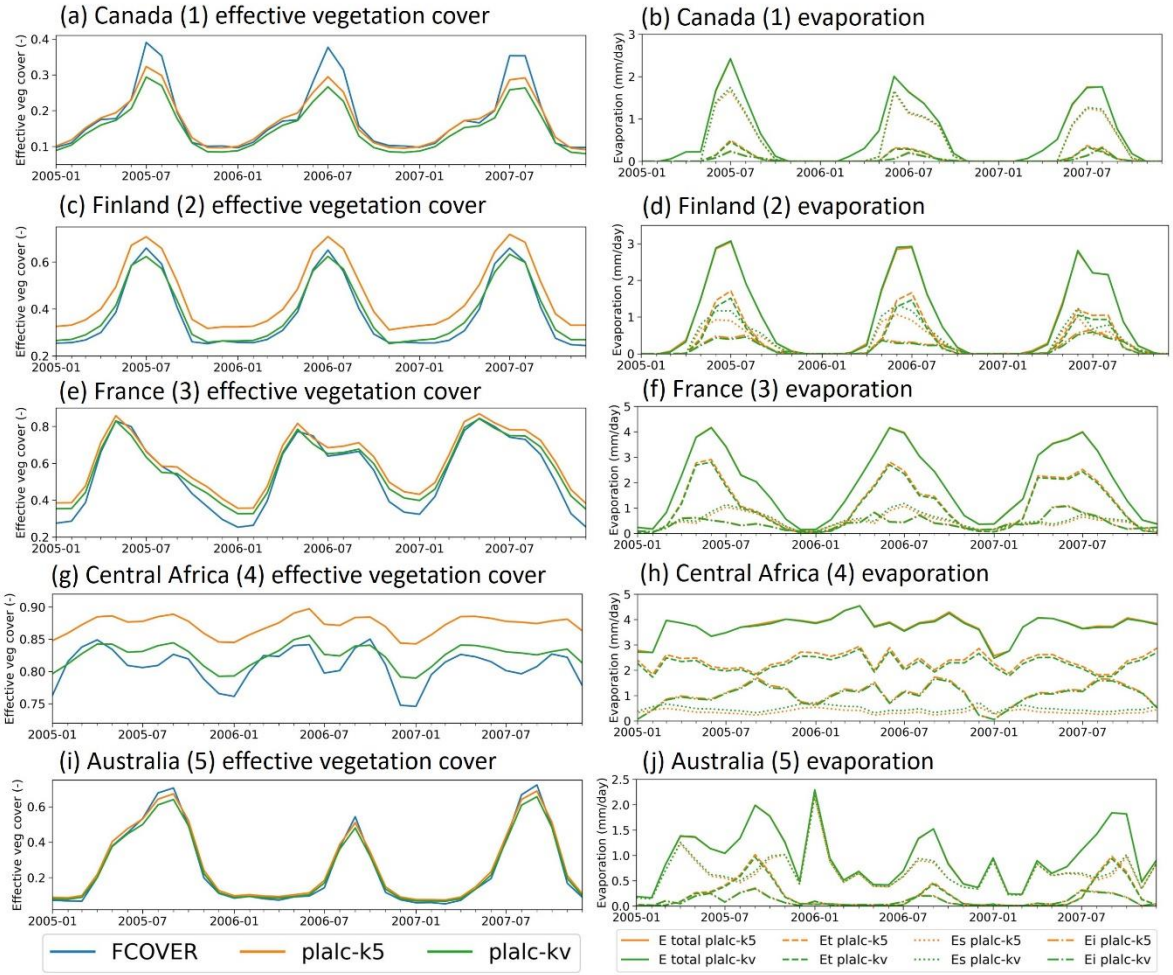

Figure 32 Timeseries for the 5 specific points pointed in the maps in Figure 30 of CVH+CVL in plalc-k5 and plalc-kv FCOVER data (a, c, e, g, i) and model evaporation with E total total evaporation, Et transpiration, Es soil evaporation and Ei interception evaporation (b, d, f, h, j).

Comparison to reference data

The implementation of CGLS LAI and ESA-CCI land cover together with the vegetation specific effective cover parameterization result in a consistent improvement of the anomaly correlation of the top layer soil moisture (Figure 33c, d) and mixed improvement and degradation for anomaly correlation of evaporation (Figure 33a, b). From the results in the previous two sections we learn that the changes observed here are mostly related to the inter-annual variability of LAI and to a lesser extent to the changes in land cover and effective cover parameterization.

Soil moisture and evaporation anomaly correlation consistently improve during dry periods in transitional climates, with predominantly low vegetation (crops and short grass) (Figure 33,Figure 27 and Figure 28). In the Sahel the anomaly correlation of evaporation increases from 0.720 in ctr-K5 to 0.784 in plalc-kv and anomaly correlation of SM increases from 0.396 to 0.429 during the dry JJA season. Similarly, correlation coefficients increase in JJA in Northeast Brazil (E: 0.760 to 0.812; SM: 0.537 to 0.639), JJA central Asia (E: 0.790 to 0.810; SM: 0.616 to 0.653) and DJF in India (E: 0.787 to 0.810; SM: 0.566 to 0.667). In these transitional areas the top layer soil moisture and evaporation are

coupled because low vegetation has shallow roots and a relatively large bare soil fraction (lower LAI, lower effective vegetation cover).

On the other hand, evaporation in areas with predominantly high vegetation origins mostly from deeper soil layers and the bare soil fraction is smaller (higher LAI, higher effective vegetation cover). Figure 33 shows that the results for boreal and tropical forests are less consistent. In the boreal forests in Eastern Canada the JJA anomaly E correlation reduces from 0.62 to 0.577, while the anomaly SM correlation does not significantly change (r=0.335).

In the tropics we also find a degradation in anomaly evaporation correlation (all seasons), which can be related to the LAI inconsistency discussed in Section 4.3.1. In tropical Africa the anomaly correlation of evaporation (all months) decreases on average from 0.572 in ctr-k5 to 0.548 in plalc-kv for the period 1993-2019. On the other hand, the anomaly correlation is 0.568 for both experiments considering the period 1999-2019. Similarly, in the West-Amazon the correlation coefficient degrades from 0.426 to 0.395 for 1993-2019 and is constant (0.407) for 1999-2019.

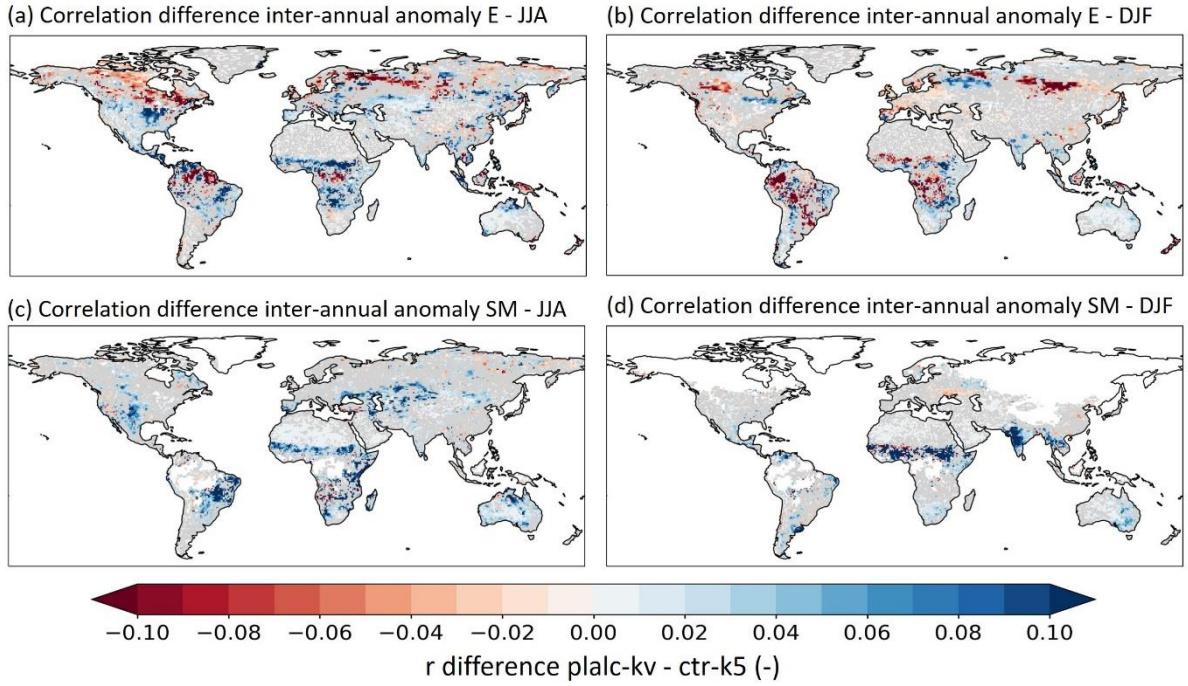

Figure 33 Correlation difference of inter annual anomaly JJA (a) and DJF (b) evaporation with respect to DOLCEv3 and JJA (c) and DJF (d) soil moisture with respect to ESA-CCI between plalc-kv and ctr-k5 for 1993-2019. Grey coloring represents non-significant (10% level) correlation difference and white represents no data available.

3.6 Multi model comparison

Here we evaluate the similarities and differences in model sensitivities in a multi model evaluation. In this model comparison we look at the effects of the inter-annual varying LAI on the model evaporation and soil moisture, using the following model experiments: MF-ctr, MF-pla, ECMWF-ctr, ECMWF-pla, CNR-ctr-kv and CNR-pla-kv (Table 3).

In this way the individual effect of the inter-annual varying LAI can be evaluated. The ECMWF and CNR ctr experiments are using climatological LAI from the novel CGLS LAI. On the other hand, the MF ctr experiment uses the ECOCLIMAP LAI and the LAI climatology in ctr and pla is therefore not the same. Model effects in MF may be also partly due to the changed climatology.

3.6.1 Evapotranspiration and soil moisture

The global and regional latent heat flux seasonal cycles (Figure 34) generally exceed the observational data (DOLCEv2) but remain within the observation uncertainty range, except for winter months over Europe where models tend to largely overestimate the latent heat flux. The MF model also overestimates this flux over the Amazon, and during spring months over the Central US. The seasonal cycle shapes are also quite well reproduced by the models, even if the ascending branch is too steep over Europe and Central US, and the peak is too early over the US (June instead of July) for all the models.

Although the CNR and ECMWF seasonal cycles are very similar in several regions as well as globally, the inter-model spread is much larger than the departure between both configurations of each model. However, configurations with inter-annual varying LAI (pla) tend to slightly improve the latent heat flux seasonality with respect to DOLCE, especially for MF at the global scale and over China.

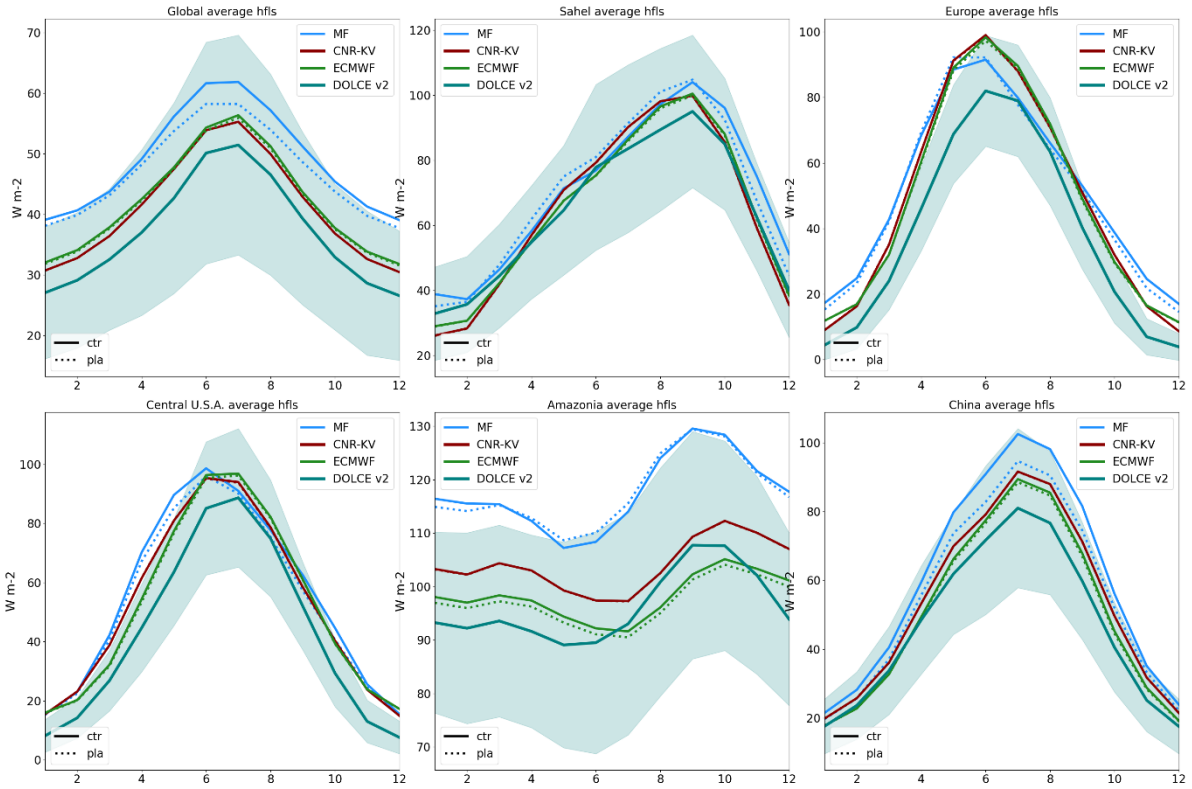

*Figure 34 Seasonal cycle of latent heat flux in DOLCEv2 (grey) and in MF (blue), CNR-KV (red) and ECMWF (green) model in control runs (ctr - solid lines), and with the prescribed vegetation (pla - dotted lines) on the period 1993-2019. The grey shading represents the uncertainties (+/- 1.64 * the standard deviation) in the estimation of the latent heat flux in DOLCE. Top left is the global average and following regions are the red boxes represented in Figure 6.*

The inter-annual variability of the latent heat flux over the same regions is shown in Figure 35. At the global scale, for the three models, configurations with inter-annual varying LAI lead to better latent heat flux correlation. The improvement is also noticeable over China, for which extreme anomalies such as 1999 (extreme low) or 2013 (extreme high) seem to be better captured by models. Over Sahel and Europe, characterized by strong and opposite trends, the correlations are high already, and the pla simulations do not substantially improve the latent heat flux variability. Correlations are also substantially increased over the Central US, but to a lesser extent for the MF model which tends to overestimate the amplitude of some of the strongest anomalies.

The case of the Amazon region is particular. Despite an overall improvement of latent heat flux variability in all pla simulations, the anomalies are largely underestimated prior to 1999, for the 3 models. This underestimation, which does not concern the ctr simulations, is probably related to the discontinuity identified in CGLS LAI time series near the equator between 1998 and 1999, and also mentioned earlier in this document.

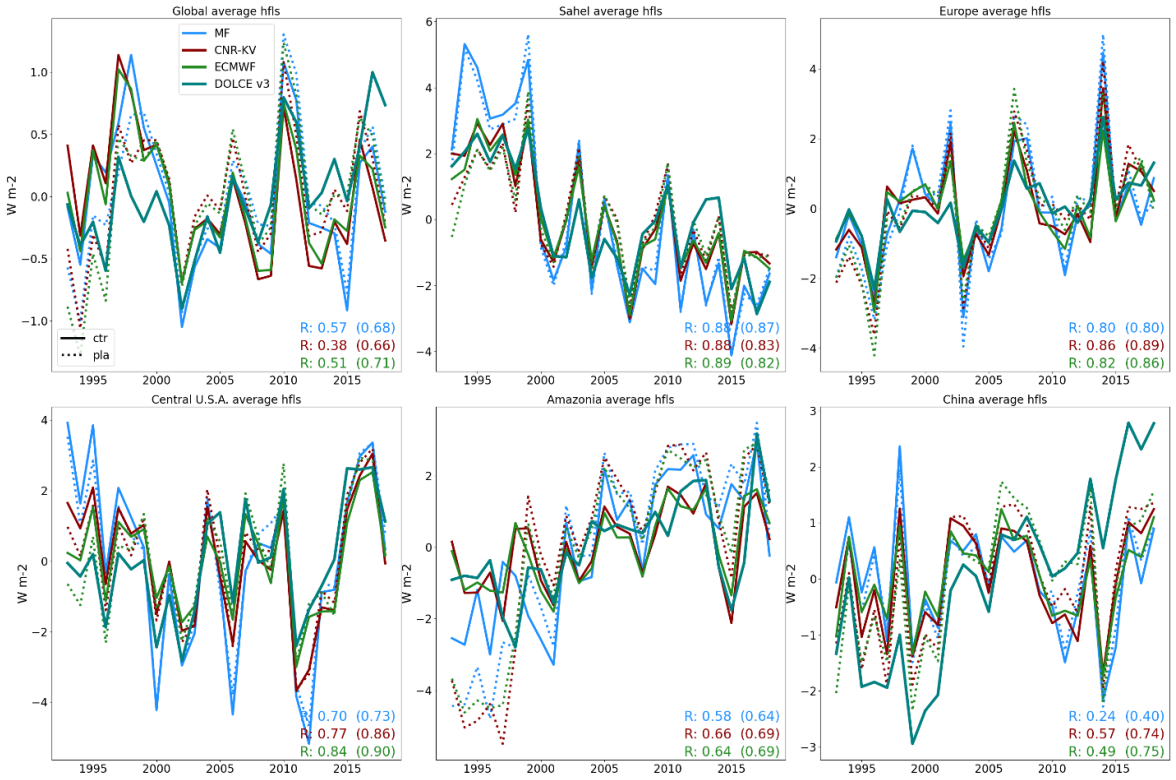

Figure 35 Same as Figure 34 for the inter-annual mean. Figures in colors show the correlation coefficient between the control experiments and DOLCEv3, figures in brackets show the correlation coefficient between the pla experiments and DOLCEv3.

The global maps of inter-annual anomaly correlation of evaporation with respect to DOLCEv3 (Figure 36) for ECMWF and CNR models show a general improvement (except for boreal and tropical forests), but the effect in ECMWF is larger. On the other hand, the MF model shows different effects with a decrease in correlations for MF-pla over Europe, Western North America and South-East Asia. Interestingly, in contrast with the correlation effect on evaporation, the effect of the inter-annually varying LAI on the correlation of soil moisture with respect to ESA-CCI SM are of opposite sign in ECMWF with respect to CNR (Figure 37). These contrasting results are caused by the different effective vegetation cover parameterization in the two models. In the ECMWF model setup, the vegetation density parameters CVL and CVH come from look up tables and are therefore fixed in time, whereas in the CNR model setup the vegetation density CVL and CVH vary in time as an exponential function of the LAI. This difference manifests mostly during dry periods (low LAI) in transition areas between wet and dry climates such as the Sahel, North-East Brazil, US Great Plains and Australia.

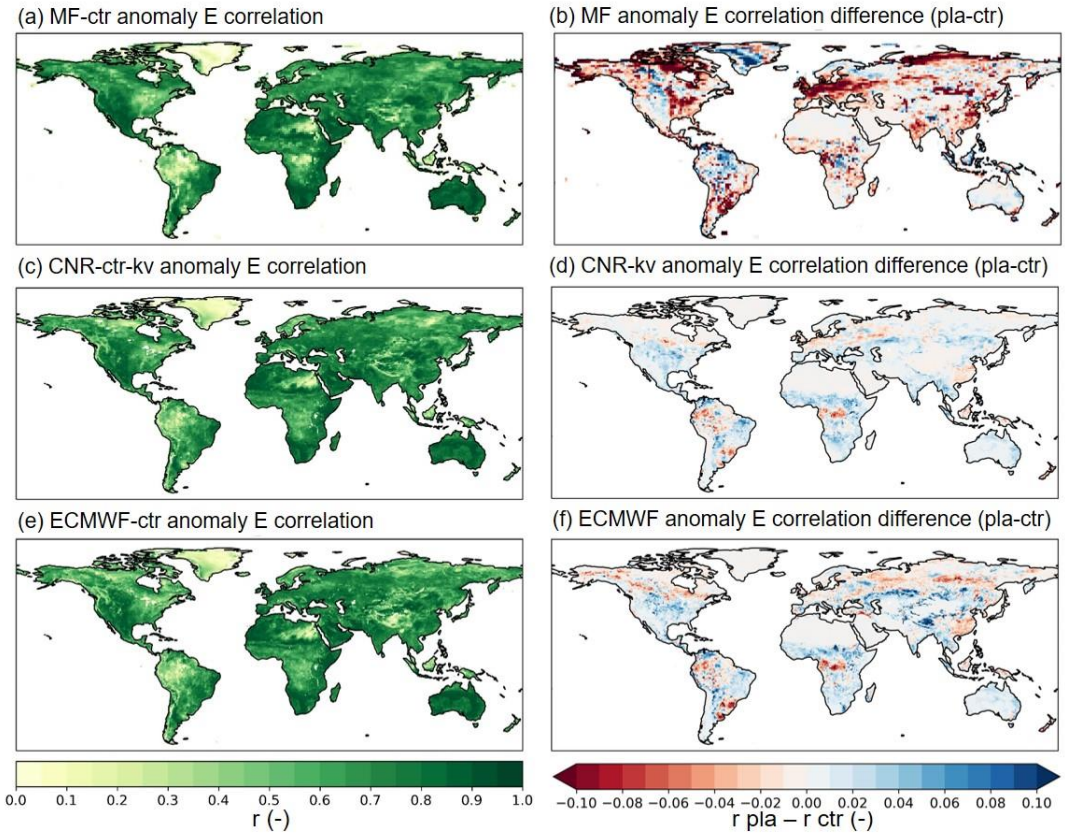

Figure 36 Correlation of detrended inter-annual anomaly evaporation with respect to DOLCEv3 evaporation for the control model (a, c, e) and the difference (pla-ctr) (b, d, f) for MF, CNR and ECMWF models for the period 1993-2018. Detrending was applied to anomaly evaporation timeseries for each month separately.

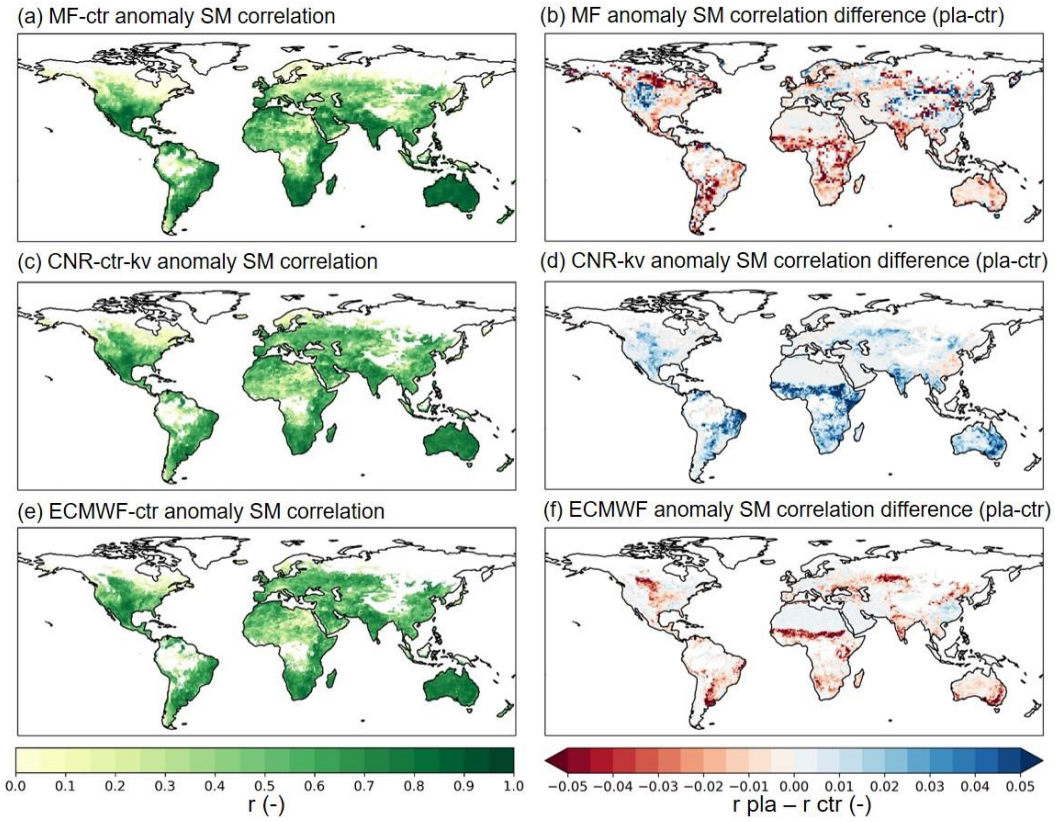

Figure 37 Correlation of detrended inter-annual anomaly top layer soil moisture with respect to ESA-CCI soil moisture for the control model (a, c, e) and the difference (pla-ctr) (b, d, f) for MF, CNR and ECMWF models for the period 1993-2019. Detrending was applied to anomaly evaporation timeseries for each month separately.

Here we zoom into a dry summer (JJA) in South US in 2011 to exemplify the effect of the inter-annually varying LAI and the effective vegetation cover parameterization on evaporation and soil moisture (Figure 38). In the CNR model, the reduction in LAI results in a reduced effective vegetation cover and an increased bare soil fraction. As a consequence, top layer soil evaporation increases and top layer soil moisture reduces. A drying of the top layer soil moisture is expected during droughts which is shown in Figure 38 in which the CNR-pla model closer matches the ESA-CCI SM than CNR-ctr. This does not happen in ECMWF and MF models, where top layer soil moisture slightly increases during a dry period. Here top layer drying does not occur because the vegetation density is fixed and as a consequence soil evaporation does not change. On the other hand, the slight increase in top layer SM can be explained by a reduction in vegetation transpiration from the top layer as a result of the reduction in prescribed LAI. For MF a similar parameterization of the vegetation density to the CNR model is used only for areas dominated by crops. This possibly explains the improvements in anomaly SM correlation in North-West US, Eastern Europe and South-East China.

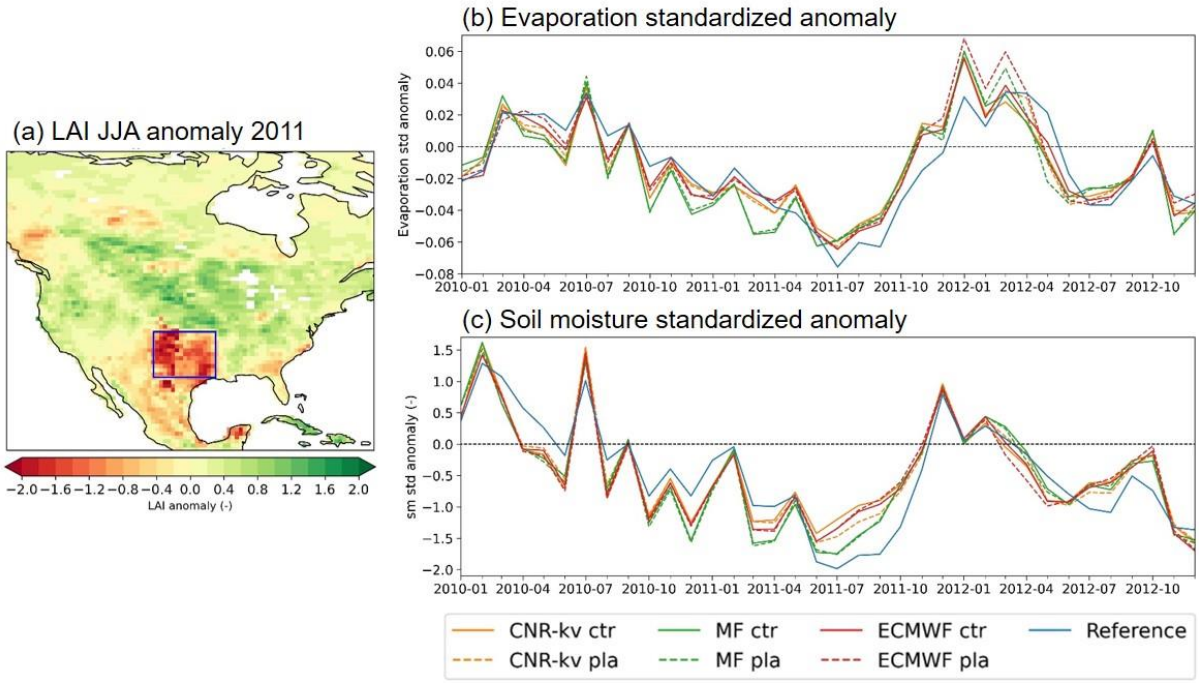

Figure 38 Drought case USA 2011 with (a) LAI JJA anomaly, (b) evaporation standardized anomalies in ctr and pla compared to DOLCEv3 and (c) soil moisture standardized anomalies in ctr and pla compared to ESA-CCI SM. Standardization is done based on the monthly standard deviations.

4 Conclusion

This report integrates the land cover and vegetation information, from the latest satellite campaigns in the frame of Copernicus, in the CHTESSEL (ECMWF), the EC-Earth HTESSEL-LPJGuess (CNR) and the ISBA-CTRIP (Météo-France) land surface models used for reanalysis and initialization of the seasonal-to-decadal prediction systems. The integration of satellite observations leads to a more realistic representation of vegetation seasonal and inter-annual variability and of the related interaction with the atmosphere. The overall improved realism leads to significant effects on the simulations by the LSMs when forced offline by the latest global reanalysis ERA5. The effects on surface fluxes and soil moisture content are often, but not always, improving compared with the available observations. These mixed results may be partly related to the offline model setup, in which atmospheric boundary conditions largely control the model surface fluxes. Moreover, it is possible that the land surface parameters used in these LSMs are adapted to the previous static climatological data and to the lack of vegetation variability to compensate for errors. It is suggested here that some parameters in LSMs may need to be re-adjusted to be now consistent with the improved representation of land cover and vegetation variability.

The inter-annually varying vegetation-LAI effects on surface fluxes and soil moisture content are however considerably diverse in the different LSMs, at least in part related with their diversity in the parameterization of the biophysical processes. The improvements in model evaporation are comparable for CHTESSEL and HTESSEL-LPJGuess, but the results for ISBA-CTRIP are largely different. The HTESSEL-LPJGuess LSM displays considerable improvements in the simulation of top layer soil moisture content over transition areas between wet and dry climates such as Sahel, Nordeste Brazil, US Great plains, India, and Australia. This is different from the sensitivity in CHTESSEL and ISBA-CTRIP that show negative effects of the inter-annually varying LAI over these regions. It is the effective cover parameterization implemented in the HTESSEL-LPJGuess that allows for realistic inter-annual variation of vegetation density when LAI is prescribed. This is needed in transition areas to properly control the partitioning of the different evapotranspiration-flux components (transpiration, interception evaporation and soil evaporation) that produce moisture extraction at different depths in the soil.

The knowledge from the sensitivity analysis in this report is driving the selection of the better solutions and configuration to include for the initialization/simulation of the predictions in CONFESS WP3.

5 References

Alessandri, A., Catalano, F., De Felice, M., Van Den Hurk, B., Doblas Reyes, F., Boussetta, S., ... & Miller, P. A. (2017). Multi-scale enhancement of climate prediction over land by increasing the model sensitivity to vegetation variability in EC-Earth. *Climate dynamics*, *49*(4), 1215-1237. https://doi.org/10.1007/s00382-016-3372-4

Anderson, M. C., Norman, J. M., Kustas, W. P., Li, F., Prueger, J. H., & Mecikalski, J. R. (2005). Effects of vegetation clumping on two–source model estimates of surface energy fluxes from an agricultural landscape during SMACEX. *Journal of Hydrometeorology*, *6*(6), 892-909. https://doi.org/10.1175/JHM465.1

Balsamo, G., Beljaars, A., Scipal, K., Viterbo, P., van den Hurk, B., Hirschi, M., & Betts, A. K. (2009). A revised hydrology for the ECMWF model: Verification from field site to terrestrial water storage and impact in the Integrated Forecast System. *Journal of hydrometeorology*, *10*(3), 623-643. https://doi.org/10.1175/2008JHM1068.1

Balsamo, G., S. Boussetta, E. Dutra, A. Beljaars, P. Viterbo, B. Van den Hurk, 2011: Evolution of land surface processes in the IFS, ECMWF Newsletter, 127, 17-22.

Boussetta, S., G. Balsamo, A. Beljaars, A. Agusti-Panareda, J.-C. Calvet, C. Jacobs, B. van den Hurk, P. Viterbo, S. Lafont, E. Dutra, L. Jarlan, M. Balzarolo, D. Papale, G. van der Werf, 2013: Natural land carbon dioxide exchanges in the ECMWF Integrated Forecasting System: Implementation and offline validation, J. Geophys. Res., 118, 5923–5946, DOI: 10.1002/jgrd.50488.

Boussetta, S., Balsamo, G., Beljaars, A., Kral, T., & Jarlan, L. (2013). Impact of a satellite-derived leaf area index monthly climatology in a global numerical weather prediction model. *International journal of remote sensing*, *34*(9-10), 3520-3542. https://doi.org/10.1080/01431161.2012.716543

Boussetta, S., Balsamo, G., Dutra, E., Beljaars, A., & Albergel, C. (2015). Assimilation of surface albedo and vegetation states from satellite observations and their impact on numerical weather prediction. Remote Sensing of Environment, 163(15), 111–126. https://doi.org/10.1016/j.rse.2015.03.009

Boussetta S, Balsamo G, Arduini G, Dutra E, McNorton J, Choulga M, Agustí-Panareda A, Beljaars A, Wedi N, Munõz-Sabater J, de Rosnay P, Sandu I, Hadade I, Carver G, Mazzetti C, Prudhomme C, Yamazaki D, Zsoter E. (2021). ECLand: The ECMWF Land Surface Modelling System. *Atmosphere*. 2021; 12(6):723. https://doi.org/10.3390/atmos12060723

Calvet, J. C., Noilhan, J., Roujean, J. L., Bessemoulin, P., Cabelguenne, M., Olioso, A., & Wigneron, J. P. (1998). An interactive vegetation SVAT model tested against data from six contrasting sites. *Agricultural and Forest Meteorology*, 92, 73– 95. https://doi.org/10.1016/S0168-1923(98)00091-4

Chen, J. M., Menges, C. H., & Leblanc, S. G. (2005). Global mapping of foliage clumping index using multi-angular satellite data. *Remote Sensing of Environment*, *97*(4), 447-457. https://doi.org/10.1016/j.rse.2005.05.003

Chen, J. M., Mo, G., Pisek, J., Liu, J., Deng, F., Ishizawa, M., and Chan, D. (2012), Effects of foliage clumping on the estimation of global terrestrial gross primary productivity, *Global Biogeochem. Cycles*, 26, GB1019, doi:10.1029/2010GB003996.

Decharme, B., Delire, C., Minvielle, M., Colin, J., Vergnes, J.-P., Alias, A., et al. (2019). Recent changes in the ISBA-CTRIP land surface system for use in the CNRM-CM6 climate model and in global off-line hydrological applications. *Journal of Advances in Modeling Earth Systems*, 11, 1207– 1252. https://doi.org/10.1029/2018MS001545

Delire, C., Séférian, R., Decharme, B., Alkama, R., Calvet, J.-C., Carrer, D., et al. (2020). The global land carbon cycle simulated with ISBA-CTRIP: Improvements over the last decade. *Journal of Advances in Modeling Earth Systems*, 12, e2019MS001886. https://doi.org/10.1029/2019MS001886

Dorigo, W., Wagner, W., Albergel, C., Albrecht, F., Balsamo, G., Brocca, L., ... & Lecomte, P. (2017). ESA CCI Soil Moisture for improved Earth system understanding: State-of-the art and future directions. *Remote Sensing of Environment*, *203*, 185-215. https://doi.org/10.1016/j.rse.2017.07.001

Döscher, R., Acosta, M., Alessandri, A., Anthoni, P., Arsouze, T., Bergman, T., Bernardello, R., Boussetta, S., Caron, L.-P., Carver, G., Castrillo, M., Catalano, F., Cvijanovic, I., Davini, P., Dekker, E., Doblas-Reyes, F. J., Docquier, D., Echevarria, P., Fladrich, U., Fuentes-Franco, R., Gröger, M., v. Hardenberg, J., Hieronymus, J., Karami, M. P., Keskinen, J.-P., Koenigk, T., Makkonen, R., Massonnet, F., Ménégoz, M., Miller, P. A., Moreno-Chamarro, E., Nieradzik, L., van Noije, T., Nolan, P., O'Donnell, D., Ollinaho, P., van den Oord, G., Ortega, P., Prims, O. T., Ramos, A., Reerink, T., Rousset, C., Ruprich-Robert, Y., Le Sager, P., Schmith, T., Schrödner, R., Serva, F., Sicardi, V., Sloth Madsen, M., Smith, B., Tian, T., Tourigny, E., Uotila, P., Vancoppenolle, M., Wang, S., Wårlind, D., Willén, U., Wyser, K., Yang, S., Yepes-Arbós, X., and Zhang, Q. (2022): The EC-Earth3 Earth system model for the Coupled Model Intercomparison Project 6, *Geosci. Model Dev.*, 15, 2973–3020, https://doi.org/10.5194/gmd-15-2973-2022

ECMWF: Part IV: Physical Processes, IFS Documentation, available at: https://www.ecmwf.int/node/17117 (last access: September 2022), 2021. http://dx.doi.org/10.21957/eyrpir4vj

Faroux, S., Kaptué Tchuenté, A. T., Roujean, J.-L., Masson, V., Martin, E., & Le Moigne, P. (2013). ECOCLIMAP-II/Europe: A twofold database of ecosystems and surface parameters at 1-km resolution based on satellite information for use in land surface, meteorological and climate models. *Geoscientific Model Development*, 6, 563– 582. https://doi.org/10.5194/gmd-6-563-2013

Gibelin, A.-L., Calvet, J.-C., Roujean, J.-L., Jarlan, L., & Los, S. (2006). Ability of the land surface model ISBA-A-gs to simulate leaf area index at the global scale: Comparison with satellites products. *Journal of Geophysical Research*, 111, D18102. https://doi.org/10.1029/2005JD006691

Gruber, A., Scanlon, T., van der Schalie, R., Wagner, W., and Dorigo, W. (2019). Evolution of the ESA CCI Soil Moisture climate data records and their underlying merging methodology, Earth Syst. Sci. Data, 11, 717–739, https://doi.org/10.5194/essd-11-717-2019

Hersbach, H., Bell, B., Berrisford, P., Hirahara, S., Horányi, A., Muñoz-Sabater, J., et al. (2020). The ERA5 global reanalysis. Quarterly Journal of the Royal Meteorological Society, 146(730), 1999–2049. https://doi.org/10.1002/qj.3803

Hobeichi, S., Abramowitz, G., & Evans, J. (2020). Conserving Land–Atmosphere Synthesis Suite (CLASS), Journal of Climate, 33(5), 1821-1844. https://journals.ametsoc.org/view/journals/clim/33/5/jcli-d-19-0036.1.xml

Hobeichi, S., Abramowitz, G., and Evans, J. P. (2021). Robust historical evapotranspiration trends across climate regimes, Hydrol. Earth Syst. Sci., 25, 3855–3874, https://doi.org/10.5194/hess-25-3855-2021

Hurtt, G. C., Chini, L. P., Frolking, S., et al. (2011). Harmonization of land-use scenarios for the period 1500–2100: 600 years of global gridded annual land-use transitions, wood harvest, and resulting secondary lands. *Climatic Change*, 109, 117– 161. https://doi.org/10.1007/s10584-011-0153-2

Jacobs, C. M. J. (1994), Direct impact of atmospheric CO_2 enrichment on regional transpiration, Ph.D. thesis, Agricultural University, Wageningen.

Joetzjer, E., Delire, C., Douville, H., Ciais, P., Decharme, B., Carrer, D., Verbeeck, H., De Weirdt, M., & Bonal, D. (2015). Improving the ISBACC land surface model simulation of water and carbon fluxes and stocks over the Amazon Forest. *Geoscientific Model Development*, 8, 1709– 1727. https://doi.org/10.5194/gmd-8-1709-2015

Johannsen, F., Ermida, S., Martins, J. P. A., Trigo, I. F., Nogueira, M., & Dutra, E. (2019). Cold bias of ERA5 summertime daily maximum land surface temperature over Iberian Peninsula. Remote Sensing, 11(21), 2570. https://doi.org/10.3390/rs11212570

Jung, M., Koirala, S., Weber, U., Ichii, K., Gans, F., Camps-Valls, G., Papale, D., Schwalm, C., Tramontana, G., and Reichstein, M.: The FLUXCOM ensemble of global land-atmosphere energy fluxes, Scientific Data, 6, https://doi.org/10.1038/s41597-019-0076-8, 2019.

Krinner, G., Viovy, N., de Noblet-Ducoudré, N., Ogée, J., Polcher, J., Friedlingstein, P., Ciais, P., Sitch, S., and Prentice, I. C. (2005), A dynamic global vegetation model for studies of the coupled atmosphere-biosphere system, *Global Biogeochem. Cycles*, 19, GB1015, doi:10.1029/2003GB002199.

Loveland, T. R., Reed, B. C., Brown, J. F., Ohlen, D. O., Zhu, Z., Yang, L. W. M. J., & Merchant, J. W. (2000). Development of a global land cover characteristics database and IGBP DISCover from 1 km AVHRR data. *International journal of remote sensing*, *21*(6-7), 1303-1330. https://doi.org/10.1080/014311600210191

Martens, B., Miralles, D. G., Lievens, H., van der Schalie, R., de Jeu, R. A. M., Fernández-Prieto, D., Beck, H. E., Dorigo, W. A., and Verhoest, N. E. C.: GLEAM v3: satellite-based land evaporation and root-zone soil moisture, Geosci. Model Dev., 10, 1903–1925, https://doi.org/10.5194/gmd-10-1903-2017, 2017.

Nogueira, M., Albergel, C., Boussetta, S., Johannsen, F., Trigo, I. F., Ermida, S. L., ... & Dutra, E. (2020). Role of vegetation in representing land surface temperature in the CHTESSEL (CY45R1) and SURFEX-ISBA (v8. 1) land surface models: A case study over Iberia. *Geoscientific Model Development*, *13*(9), 3975-3993. https://doi.org/10.5194/gmd-13-3975-2020

O, S. and Orth, R.: Global soil moisture data derived through machine learning trained with in-situ measurements, Scientific Data, 8, https://doi.org/10.1038/s41597-021-00964-1, 2021.

Ryu, Y., Nilson, T., Kobayashi, H., Sonnentag, O., Law, B. E., & Baldocchi, D. D. (2010). On the correct estimation of effective leaf area index: Does it reveal information on clumping effects?. *Agricultural and Forest Meteorology*, *150*(3), 463-472. https://doi.org/10.1016/j.agrformet.2010.01.009

Verger, A., Baret, F., & Weiss, M. (2019). ATBD of the Copernicus Global Land Operations "Vegetation and Energy". Copernicus Global Land Services documentations.

https://land.copernicus.eu/global/sites/cgls.vito.be/files/products/CGLOPS1_ATBD_FCOVER1km-V2_I1.41.pdf

Voldoire, A., Decharme, B., Pianezze, J., Lebeaupin Brossier, C., Sevault, F., Seyfried, L., Garnier, V., Bielli, S., Valcke, S., Alias, A., Accensi, M., Ardhuin, F., Bouin, M.-N., Ducrocq, V., Faroux, S., Giordani, H., Léger, F., Marsaleix, P., Rainaud, R., Redelsperger, J.-L., Richard, E., and Riette, S.: SURFEX v8.0 interface with OASIS3-MCT to couple atmosphere with hydrology, ocean, waves and sea-ice models, from coastal to global scales, Geosci. Model Dev., 10, 4207–4227. https://doi.org/10.5194/gmd-10-4207-2017

Document History

Version	Author(s)	Date	Changes
	Name (Organisation)	dd/mm/yyyy	
V0	Fransje van Oorschot (CNR) Andrea Alessandri (CNR) Constantin Ardilouze (MF) Gildas Dayon (MF)	07/09/2022	Report structure + first results
V1	Fransje van Oorschot (CNR) Andrea Alessandri (CNR) Constantin Ardilouze (MF) Gildas Dayon (MF) Souhail Boussetta (ECMWF) Gianpaolo Balsamo (ECMWF) Melissa Ruiz-Vasquez (ECMWF	30/09/2022	Finalization of results and methods
V2	Fransje van Oorschot (CNR) Andrea Alessandri (CNR) Constantin Ardilouze (MF) Gildas Dayon (MF) Souhail Boussetta (ECMWF) Gianpaolo Balsamo (ECMWF) Melissa Ruiz-Vasquez (ECMWF)	07/10/2022	Finalization of Executive Summary, Introduction and Conclusions; refinement of text and figures.
V3	Fransje van Oorschot (CNR) Andrea Alessandri (CNR)	28/10/2022	Processing review comments BSC

Internal Review History

Internal Reviewers	Date	Comments
Name (Organisation)	dd/mm/yyyy	
Etienne Tourigny (BSC)	27/10/2022	See CONFESS_D1-2-V2.0_final-Etienne.docx

Estimated Effort Contribution per Partner

Partner	Effort
CNR	11
ECMWF	7
MF	11
Total	29